Comput Mech (2017) 59:753–778
DOI 10.1007/s00466-016-1371-2

ORIGINAL PAPER

Hyper-reduction of generalized continua

Martin Horák[1] · **David Ryckelynck**[1] · **Samuel Forest**[1]

Received: 19 May 2016 / Accepted: 20 December 2016 / Published online: 30 January 2017

Abstract This paper deals with the reduced order modeling of micromorphic continua. The reduced basis model relies on the proper orthogonal decomposition and the hyper-reduction. Two variants of creation of reduced bases using the proper orthogonal decomposition are explored from the perspective of additional micromorphic degrees of freedom. In the first approach, one snapshot matrix including displacement as well as micromorphic degrees of freedom is assembled. In the second approach, snapshots matrices are assembled separately for displacement and micromorphic fields and the singular value decomposition is performed on each system separately. Thereafter, the formulation is extended to the hyper-reduction method. It is shown that the formulation has the same structure as for the classical continua. The relation of higher order stresses introduced in micromorphic balance equations to creation of the reduced integration domain is examined. Finally, the method is applied to examples of microdilatation extension and clamped tension and to a size-dependent stress concentration in Cosserat elasticity. It is shown that the proposed approach leads to a good level of accuracy with significant reduction of computational time.

Keywords Reduced order modeling · POD · Hyper-reduction · Reduced integration domain · Micromorphic continua · Generalized continua · Cosserat continuum

✉ David Ryckelynck
david.ryckelynck@mines-paristech.fr

[1] Centre des Matériaux, CNRS UMR 7633, Mines, Paristech, BP 87, 91003 Evry Cedex, France

1 Introduction

The classical continuum theory fails to describe certain mechanical phenomena such as dispersion of elastic waves, size effects on material properties, or strain softening of materials. To capture these phenomena, the theory needs to be enhanced. One possible remedy is based on the so-called micromorphic formulation which introduces one or several material length scale parameters, see [1–3] to cite but a few. Within this approach, each macroscopic material point is embedded with a microscopic system that has its own kinematic field, i.e., additional degrees of freedom, describing the micro-deformation. A coupling between macro- and micro-scale is provided via a balance of micromorphic stresses which are energetically conjugated to the difference between micro-deformation and macro-deformation and to the gradient of the micro-field. Note that the term micromorphic is used here in a broad sense and incorporates the micropolar, microstretch, second-gradient, or couple-stress theories among others, as special cases, see [4].

The micromorphic approach introduces several new degrees of freedom hence the formulation leads to a computationally demanding problem. Model reduction such as the reduced basis method [5,6] and proper orthogonal decomposition (POD) can be used to reduce computational costs when parametric study is necessary to set-up convenient material constants. However, these methods reduces only the number of equations to be solved and has no effect on the integration of the constitutive equations which may be very time-consuming and can constitute more than half of total computational time. Hyper-reduction introduced in [7] solves this issue by adopting a reduced integration domain, namely a small part of the original domain over which the constitutive equations are integrated, and thus leads to a drastic reduction of computational costs of the reduced solution. The hyper-

reduction has been successfully used for several problems, including models with internal variables [8] or large-strain plasticity [9]. Additionally, in [10], the method was applied to a multi-scale problem with the hyper-reduced RVE scale. For these reasons, the present work focuses on the formulation of a reduced-order model of generalized continua based on the POD and hyper-reduction. The POD applied to dynamics of rods and shells which can be considered as lower-order Cosserat continua can be found for example in [11] or [12]. However, we present to our best knowledge for the first time a general linear theory applicable to 3D problems and to other types of micromorphic continua such as microdilatation one or even to continua with gradient of internal parameters [13]. In addition, the formulation is extended to the hyper-reduction method.

The layout of the paper is as follows. In Sect. 2, we outline a general approach to micromorphic continua and its finite element formulation is briefly presented. A simple constitutive framework is considered, based on a generalized isotropic elasticity with two new material parameters. The theory is presented within the small-strain framework. In Sect. 3, reduced order modeling of micromorphic continua based on the proper orthogonal decomposition and hyper-reduction is introduced. Finally, in Sect. 4, we explore the proposed methodology using three numerical examples. Although the proposed examples have an affine parameter dependence suitable for the implementation of the reduced basis method, we have consider them as a first stage before application of the hyper-reduction to non-linear micromorphic problems that, in general, do not have affine parameter dependence.

Notation

The zeroth, first, second, third, and fourth order tensors are denoted by $a, \underline{a}, \underset{\sim}{a}, \underline{\underline{a}}$, and $\underset{\sim}{\underline{\underline{a}}}$, respectively. The dyadic product is designated as $\otimes$, the simple, double, and triple contraction are denoted as $\cdot$, $:$, $\vdots$ and they are defined through the index notation with respect to an orthonormal Cartesian basis where the Einstein summation rule applies:

$$(\underline{a} \otimes \underline{b})_{ij} = a_i b_j, \quad \underline{a} \cdot \underline{b} = a_i b_i,$$
$$\underset{\sim}{a} : \underline{b} = a_{ij} b_{ij}, \quad \underline{\underline{a}} \vdots \underline{\underline{b}} = a_{ijk} b_{ijk}$$

Using an orthonormal basis, the gradient and the divergence are expressed as:

$$(\nabla \underline{a})_{ijk} = \frac{\partial a_{ij}}{\partial x_k}, \quad (\operatorname{div} \underline{a})_i = \frac{\partial a_{ij}}{\partial x_j}, \quad (\operatorname{div} \underline{\underline{M}})_{ij} = \frac{\partial M_{ijk}}{\partial x_k}$$

The tensorial notation is very practical for theoretical developments; however, a matrix notation is more convenient for the numerical implementation. Therefore, the matrix notation is used to describe finite element implementation. Bold lower-case letters such as **a** are used for arrays, while matrices are denoted by bold capital letters, e.g., **A**.

2 Micromorphic continua

The micromorphic continua, introduced in [1–3], is a class of generalized continua that contains several well-known continua such as the Cosserat continuum or continua with gradient of some internal variables [13]. These continua incorporate a feature of the microstructure by refining the kinematics by additional degrees of freedom. Using the notation from [13], the new degrees of freedom ${}^{\chi}\underset{\sim}{\boldsymbol{\phi}}$ and their gradient $\nabla {}^{\chi}\underset{\sim}{\boldsymbol{\phi}}$ are introduced in the power of internal forces together with their dual variables, namely the relative stress tensor $\underset{\sim}{\boldsymbol{S}}$ and double stress tensor $\underline{\underline{\boldsymbol{M}}}$.

2.1 Principle of virtual power

The method of virtual power provides a very powerful and systematic way of deriving balance equations of micromorphic continua, see [14,15].

The power of internal virtual forces is enriched as

$$\mathcal{P}^{(i)}(\underline{\dot{\boldsymbol{u}}}^{\star}, {}^{\chi}\underset{\sim}{\dot{\boldsymbol{\phi}}}^{\star}) = -\int_{\mathcal{D}} p^{(i)}(\underline{\dot{\boldsymbol{u}}}^{\star}, {}^{\chi}\underset{\sim}{\dot{\boldsymbol{\phi}}}^{\star})\, dV,$$
$$p^{(i)}(\underline{\dot{\boldsymbol{u}}}^{\star}, {}^{\chi}\underset{\sim}{\dot{\boldsymbol{\phi}}}^{\star}) = \underset{\sim}{\boldsymbol{\sigma}} : \nabla \underline{\dot{\boldsymbol{u}}}^{\star} + \underset{\sim}{\boldsymbol{S}} : {}^{\chi}\underset{\sim}{\dot{\boldsymbol{\phi}}}^{\star} + \underline{\underline{\boldsymbol{M}}} \vdots \nabla {}^{\chi}\underset{\sim}{\dot{\boldsymbol{\phi}}}^{\star} \tag{1}$$

where $\underline{\dot{\boldsymbol{u}}}^{\star}, {}^{\chi}\underset{\sim}{\dot{\boldsymbol{\phi}}}^{\star}$ are virtual velocities and $\mathcal{D}$ is a subdomain of the body Ω.

In general, the virtual power of external forces could be enhanced by terms that correspond to generalized body forces, but to keep the presentation simple we introduce only generalized tractions $\underset{\sim}{\boldsymbol{t}}_M$

$$\mathcal{P}^{(e)}(\underline{\dot{\boldsymbol{u}}}^{\star}, {}^{\chi}\underset{\sim}{\dot{\boldsymbol{\phi}}}^{\star}) = \int_{\mathcal{D}} \underline{\boldsymbol{b}} \cdot \underline{\dot{\boldsymbol{u}}}^{\star}\, dV + \int_{\partial\mathcal{D}} \underline{\boldsymbol{t}}_{\sigma} \cdot \underline{\dot{\boldsymbol{u}}}^{\star}\, d\Gamma + \int_{\partial\mathcal{D}} \underset{\sim}{\boldsymbol{t}}_M : {}^{\chi}\underset{\sim}{\dot{\boldsymbol{\phi}}}^{\star}\, d\Gamma \tag{2}$$

where $\underline{\boldsymbol{b}}$ and $\underline{\boldsymbol{t}}_{\sigma}$ are the standard body forces and tractions, $\partial\mathcal{D}$ represents the boundary of the subdomain $\mathcal{D}$.

The principle of virtual power states that:

$$\mathcal{P}^{(i)}(\underline{\dot{\boldsymbol{u}}}^{\star}, {}^{\chi}\underset{\sim}{\dot{\boldsymbol{\phi}}}^{\star}) + \mathcal{P}^{(e)}(\underline{\dot{\boldsymbol{u}}}^{\star}, {}^{\chi}\underset{\sim}{\dot{\boldsymbol{\phi}}}^{\star}) = 0, \ \forall \mathcal{D} \subset \Omega, \ \forall \underline{\dot{\boldsymbol{u}}}^{\star}, {}^{\chi}\underset{\sim}{\dot{\boldsymbol{\phi}}}^{\star} \tag{3}$$

The principle of virtual power leads to the standard equilibrium equation and to a balance equation for the micromorphic stresses:

$$\operatorname{div} \underset{\sim}{\boldsymbol{\sigma}} + \underline{\boldsymbol{b}} = \underline{\mathbf{0}}, \quad \forall \underline{\boldsymbol{x}} \in \Omega \tag{4}$$

$$\operatorname{div} \underset{\approx}{\boldsymbol{M}} - \underset{\sim}{\boldsymbol{S}} = \underline{\mathbf{0}}, \quad \forall \underline{\boldsymbol{x}} \in \Omega \tag{5}$$

Associated boundary conditions for the simple and generalized tractions read

$$\underset{\sim}{\boldsymbol{\sigma}}.\underline{\boldsymbol{n}} = \underline{\boldsymbol{t}}_{\sigma}, \quad \forall \underline{\boldsymbol{x}} \in \partial\mathcal{D} \tag{6}$$

$$\underset{\approx}{\boldsymbol{M}}.\underline{\boldsymbol{n}} = \underline{\boldsymbol{t}}_{M}, \quad \forall \underline{\boldsymbol{x}} \in \partial\mathcal{D} \tag{7}$$

2.2 Constitutive equations

For simplicity, the attention is restricted to linear isotropic elasticity. The free energy density function ψ is chosen as a function of a generalized relative strain variable $\underset{\sim}{\boldsymbol{e}}$ defined as:

$$\underset{\sim}{\boldsymbol{e}} = \underset{\sim}{\boldsymbol{\phi}} - {}^{\chi}\underset{\sim}{\boldsymbol{\phi}} \tag{8}$$

where $\underset{\sim}{\boldsymbol{\phi}}$ is a macroscopic variable to be selected. The free energy can be decomposed into classical and micromorphic parts $\psi^{(1)}$ and $\psi^{(2)}$ where

$$\psi(\nabla\underline{\boldsymbol{u}}, {}^{\chi}\underset{\sim}{\boldsymbol{\phi}}, \nabla {}^{\chi}\underset{\sim}{\boldsymbol{\phi}}) = \psi^{(1)}(\nabla\underline{\boldsymbol{u}}) + \psi^{(2)}(\underset{\sim}{\boldsymbol{e}}, \nabla {}^{\chi}\underset{\sim}{\boldsymbol{\phi}}) \tag{9}$$

Moreover, the following concrete forms were used

$$\rho\psi^{(1)} = \frac{1}{2}\nabla\underline{\boldsymbol{u}} : \underset{\approx}{\boldsymbol{E}} : \nabla\underline{\boldsymbol{u}} = \frac{1}{2}\lambda \operatorname{Tr}[\nabla\underset{\sim}{\boldsymbol{\varepsilon}}]^2 + \mu \operatorname{Tr}[(\nabla\underset{\sim}{\boldsymbol{\varepsilon}})^2] \tag{10}$$

$$\rho\psi^{(2)} = \frac{1}{2}H_{\chi}(\underset{\sim}{\boldsymbol{\phi}} - {}^{\chi}\underset{\sim}{\boldsymbol{\phi}})^2 + \frac{1}{2}A_{\chi}\nabla {}^{\chi}\underset{\sim}{\boldsymbol{\phi}} \cdot \nabla {}^{\chi}\underset{\sim}{\boldsymbol{\phi}} \tag{11}$$

where $\underset{\sim}{\boldsymbol{\varepsilon}}$ is the small strain tensor, $\underset{\approx}{\boldsymbol{E}}$ is the isotropic fourth-order elasticity tensor which can be expressed using Lamé parameters λ and μ, H_{χ} [MPa] is a modulus providing coupling between the macroscopic and micromorphic problems, and A [MPa mm^2] is a modulus incorporating an internal length scale. A more general constitutive law with sixth-order constitutive tensor could be used, see for example [16,17].

Assuming that the entropy principle in its classical form applies

$$-\rho\dot{\psi} + p^{(i)} \geq 0 \tag{12}$$

the state laws are derived as

$$\underset{\sim}{\boldsymbol{\sigma}} = \rho\frac{\partial\psi}{\partial\nabla\underline{\boldsymbol{u}}} = \underset{\approx}{\boldsymbol{E}} : \nabla\underline{\boldsymbol{u}} + H_{\chi}(\underset{\sim}{\boldsymbol{\phi}} - {}^{\chi}\underset{\sim}{\boldsymbol{\phi}}) : \frac{\partial\underset{\sim}{\boldsymbol{\phi}}}{\partial\nabla\underline{\boldsymbol{u}}} \tag{13}$$

$$\underset{\sim}{\boldsymbol{S}} = \rho\frac{\partial\psi}{\partial {}^{\chi}\underset{\sim}{\boldsymbol{\phi}}} = H_{\chi}({}^{\chi}\underset{\sim}{\boldsymbol{\phi}} - \underset{\sim}{\boldsymbol{\phi}}) \tag{14}$$

$$\underset{\approx}{\boldsymbol{M}} = \rho\frac{\partial\psi}{\partial\nabla {}^{\chi}\underset{\sim}{\boldsymbol{\phi}}} = A_{\chi}\nabla {}^{\chi}\underset{\sim}{\boldsymbol{\phi}} \tag{15}$$

It is worth mentioning that the stress tensors $\underset{\sim}{\boldsymbol{\sigma}}$ and $\underset{\sim}{\boldsymbol{S}}$ are generally non-symmetric. After inserting the state laws (14) and (15) into the micromorphic balance equation (5) we obtain a Helmholtz-like differential equation

$${}^{\chi}\underset{\sim}{\boldsymbol{\phi}} - l_{\chi}^2\Delta {}^{\chi}\underset{\sim}{\boldsymbol{\phi}} = \underset{\sim}{\boldsymbol{\phi}} \tag{16}$$

where Δ stands for the Laplace operator and an internal length l_{χ} is defined by

$$l_{\chi} = \sqrt{\frac{A_{\chi}}{H_{\chi}}} \tag{17}$$

The last step to complete the micromorphic formulation is the selection of the state variable $\underset{\sim}{\boldsymbol{\phi}}$. In the following sections, it is shown how to choose this variable to obtain the microdilatation and Cosserat continua.

2.3 Microdilation continuum

The microdilatation continuum [4,18] introduces one new degree of freedom which is related to the change of volume. The state variable is chosen as

$$\underset{\sim}{\boldsymbol{\phi}} = \operatorname{Tr}[\underset{\sim}{\boldsymbol{\varepsilon}}]\underset{\sim}{\mathbf{1}} \tag{18}$$

thus the medium is endowed with a micro-deformation field having a simple form

$${}^{\chi}\underset{\sim}{\boldsymbol{\phi}} = \chi\,\underset{\sim}{\mathbf{1}} \tag{19}$$

and the fields to solve are a displacement vector $\underline{\boldsymbol{u}}$ and a scalar microdilatation χ

$$DOF = \{\underline{\boldsymbol{u}}, \quad \chi\} \tag{20}$$

After exploiting the spherical form of the macroscopic field $\underset{\sim}{\boldsymbol{\phi}}$ and the micromorphic field ${}^{\chi}\underset{\sim}{\boldsymbol{\phi}}$, Eq. (5) can be simplified using lower order tensors:

$$\operatorname{div} \underline{\boldsymbol{M}}_V - S_V = 0, \quad \forall \underline{\boldsymbol{x}} \in \Omega \tag{21}$$

where $\underline{\boldsymbol{M}}_V = \underset{\approx}{\boldsymbol{M}} : \underset{\sim}{\mathbf{1}}$ and $S_V = \underset{\sim}{\boldsymbol{S}} : \underset{\sim}{\mathbf{1}}$.

Finally, the constitutive equations can be expressed by

$$\underset{\sim}{\boldsymbol{\sigma}} = \underset{\approx}{\boldsymbol{E}} : \nabla\underline{\boldsymbol{u}} + H_{\chi}(\operatorname{Tr}[\underset{\sim}{\boldsymbol{\varepsilon}}] - \chi)\underset{\approx}{\boldsymbol{I}} \tag{22}$$

$$S_V = H_{\chi}(\chi - \operatorname{Tr}[\underset{\sim}{\boldsymbol{\varepsilon}}]) \tag{23}$$

$$\underline{\boldsymbol{M}}_V = A_{\chi}\nabla\chi \tag{24}$$

Observe that the stress tensors are symmetric for this continuum.

2.4 Cosserat continuum

In the Cosserat continuum theory [19], the macroscopic variable $\underset{\sim}{\boldsymbol{\phi}}$ is chosen as a rotation $\underset{\sim}{\boldsymbol{w}}$ which is equal to the skew-symmetric part of the displacement gradient. Therefore, each material point is attached with a triad of rigid directions, i.e., each material point can rotate with the micro-rotation ${}^{\chi}\underset{\sim}{\boldsymbol{w}}$ which plays the role of the micro-variable ${}^{\chi}\underset{\sim}{\boldsymbol{\phi}}$. Degrees of freedom are extended as

$$DOF = \{\underline{\boldsymbol{u}},\ {}^{\chi}\underset{\sim}{\boldsymbol{w}}\} \tag{25}$$

and the power of internal virtual forces is then expressed as:

$$p^{(i)}(\dot{\underline{\boldsymbol{u}}}^{\star}, {}^{\chi}\dot{\underset{\sim}{\boldsymbol{w}}}^{\star}) = \underset{\sim}{\boldsymbol{\sigma}} : \nabla\dot{\underline{\boldsymbol{u}}}^{\star} + \underset{\sim}{\boldsymbol{S}} : {}^{\chi}\dot{\underset{\sim}{\boldsymbol{w}}}^{\star} + \underset{\approx}{\boldsymbol{M}} \vdots \nabla\,{}^{\chi}\dot{\underset{\sim}{\boldsymbol{w}}}^{\star} \tag{26}$$

The principle of objectivity requires that the power of internal virtual forces (26) is invariant with respect to any infinitesimal virtual rigid body motions. Under the rigid body motion, the gradient of velocity field and the rate of Cosserat rotation are changed to:

$$\nabla\dot{\underline{\boldsymbol{u}}}^{*} \leftarrow \nabla\dot{\underline{\boldsymbol{u}}}^{*} + \underset{\sim}{\boldsymbol{v}} \tag{27}$$

$${}^{\chi}\dot{\underset{\sim}{\boldsymbol{w}}}^{*} \leftarrow {}^{\chi}\dot{\underset{\sim}{\boldsymbol{w}}}^{*} + \underset{\sim}{\boldsymbol{v}} \tag{28}$$

where $\underset{\sim}{\boldsymbol{v}}$ is a skew-symmetric tensor describing rate of an infinitesimal change of observer. Therefore, the Cauchy stress tensor $\boldsymbol{\sigma}$ is non-symmetric and its skew-symmetric part $\underset{\sim}{\boldsymbol{\sigma}}^{a}$ is related to the relative stress tensors as

$$\underset{\sim}{\boldsymbol{\sigma}}^{a} = -\underset{\sim}{\boldsymbol{S}} \tag{29}$$

The following relations between a skew–symmetric tensor $\underset{\sim}{\boldsymbol{w}}$ and its axial vector $\underline{\boldsymbol{\varphi}}$ hold:

$$\underset{\sim}{\boldsymbol{w}} = -\underset{\approx}{\boldsymbol{\epsilon}} \cdot \underline{\boldsymbol{\varphi}} \qquad \underline{\boldsymbol{\varphi}} = -\frac{1}{2}\underset{\sim}{\boldsymbol{w}} : \underset{\approx}{\boldsymbol{\epsilon}} \tag{30}$$

where $\underset{\approx}{\boldsymbol{\epsilon}}$ is the permutation tensor. Substituting relations (30) back to (26) we arrive at

$$p^{(i)}(\dot{\underline{\boldsymbol{u}}}^{\star}, {}^{\chi}\dot{\underset{\sim}{\boldsymbol{\omega}}}^{\star}) = \underset{\sim}{\boldsymbol{\sigma}} : \nabla\dot{\underline{\boldsymbol{u}}}^{\star} + 2\underline{\boldsymbol{s}} \cdot {}^{\chi}\dot{\underline{\boldsymbol{\varphi}}}^{\star} + \underset{\sim}{\boldsymbol{m}} \cdot \nabla\,{}^{\chi}\dot{\underline{\boldsymbol{\varphi}}}^{\star} \tag{31}$$

where $\underline{\boldsymbol{s}}$ is the axial vector of the tensor $\underset{\sim}{\boldsymbol{S}}$

$$\underline{\boldsymbol{s}} = -\frac{1}{2}\underset{\approx}{\boldsymbol{\epsilon}} : \underset{\sim}{\boldsymbol{S}} \tag{32}$$

and the second-order tensor $\underset{\sim}{\boldsymbol{m}}$ is defined as:

$$\underset{\sim}{\boldsymbol{m}} = -\underset{\approx}{\boldsymbol{\epsilon}} : \underset{\approx}{\boldsymbol{M}} \tag{33}$$

Therefore, the set of degrees of freedom can be written as

$$DOF = \{\underline{\boldsymbol{u}},\ {}^{\chi}\underline{\boldsymbol{\varphi}}\} \tag{34}$$

and the equilibrium equations (4)–(5) can be written as

$$\operatorname{div}\underset{\sim}{\boldsymbol{\sigma}} + \underline{\boldsymbol{b}} = \underline{\boldsymbol{0}}, \quad \forall\underline{\boldsymbol{x}} \in \Omega \tag{35}$$

$$\operatorname{div}\underset{\sim}{\boldsymbol{m}} - 2\underline{\boldsymbol{s}} = \underline{\boldsymbol{0}}, \quad \forall\underline{\boldsymbol{x}} \in \Omega \tag{36}$$

Finally, the micromorphic part of the free energy is expressed as

$$\rho\psi^{(2)} = H_{\chi}({}^{\chi}\underline{\boldsymbol{\varphi}} - \underline{\boldsymbol{\varphi}}) \cdot ({}^{\chi}\underline{\boldsymbol{\varphi}} - \underline{\boldsymbol{\varphi}}) + \frac{1}{2}A_{\chi}\nabla\,{}^{\chi}\underline{\boldsymbol{\varphi}} : \nabla\,{}^{\chi}\underline{\boldsymbol{\varphi}} \tag{37}$$

Accordingly, following constitutive equations are obtained

$$\underset{\sim}{\boldsymbol{\sigma}} = \underset{\approx}{\boldsymbol{E}} : \nabla\underline{\boldsymbol{u}} + H_{\chi}\underset{\approx}{\boldsymbol{\epsilon}} \cdot ({}^{\chi}\underline{\boldsymbol{\varphi}} - \underline{\boldsymbol{\varphi}}) \tag{38}$$

$$\underline{\boldsymbol{s}} = H_{\chi}({}^{\chi}\underline{\boldsymbol{\varphi}} - \underline{\boldsymbol{\varphi}}) \tag{39}$$

$$\underset{\sim}{\boldsymbol{m}} = A_{\chi}\nabla\,{}^{\chi}\underline{\boldsymbol{\varphi}} \tag{40}$$

It is worth noting that the general form of isotropic Cosserat elasticity can be expressed as

$$\begin{aligned}\underset{\sim}{\boldsymbol{m}} = {} & \alpha\operatorname{Tr}[\nabla\,{}^{\chi}\underline{\boldsymbol{\varphi}}]\underset{\sim}{\boldsymbol{1}} + \beta\left(\nabla\,{}^{\chi}\underline{\boldsymbol{\varphi}} + (\nabla\,{}^{\chi}\underline{\boldsymbol{\varphi}})^{T}\right) \\ & + \gamma\left(\nabla\,{}^{\chi}\underline{\boldsymbol{\varphi}} - (\nabla\,{}^{\chi}\underline{\boldsymbol{\varphi}})^{T}\right)\end{aligned} \tag{41}$$

State equation (40) can be obtained from (41) by special choice of material parameters, namely $\alpha = 0$ and $\beta = \gamma = A_{\chi}/2$. See [20] for more details.

2.5 Finite element formulation

In this section, the finite element implementation of the micromorphic theory is briefly presented. The weak form of Eqs. (4) and (5) is obtained from the principle of virtual power (3) by restricting virtual fields $\dot{\underline{\boldsymbol{u}}}^{\star}, {}^{\chi}\dot{\underset{\sim}{\boldsymbol{\phi}}}^{\star}$ to zero on Dirichlet boundary Γ_u and Γ_{χ}, respectively. The problem may be stated as: Find $\underline{\boldsymbol{u}}$ and ${}^{\chi}\underset{\sim}{\boldsymbol{\phi}}$ such that, $\forall\dot{\underline{\boldsymbol{u}}}^{\star}, {}^{\chi}\dot{\underset{\sim}{\boldsymbol{\phi}}}^{\star}$

$$\begin{aligned}\int_{\mathcal{D}} \underset{\sim}{\boldsymbol{\sigma}} : \nabla\dot{\underline{\boldsymbol{u}}}^{\star} + \mathbf{S} : {}^{\chi}\dot{\underset{\sim}{\boldsymbol{\phi}}}^{\star} + \underset{\approx}{\boldsymbol{M}} \vdots \nabla\,{}^{\chi}\dot{\underset{\sim}{\boldsymbol{\phi}}}^{\star}\, dV = {} & \int_{\mathcal{D}} \underline{\boldsymbol{b}} \cdot \dot{\underline{\boldsymbol{u}}}^{\star}\, dV \\ & + \int_{\partial\mathcal{D}} \underline{\boldsymbol{t}} \cdot \dot{\underline{\boldsymbol{u}}}^{\star}\, d\Gamma + \int_{\partial\mathcal{D}} \underset{\sim}{\boldsymbol{t}}_{M} : {}^{\chi}\dot{\underset{\sim}{\boldsymbol{\phi}}}^{\star}\, d\Gamma\end{aligned} \tag{42}$$

Prior to the finite element approximation of the virtual work statement, we assemble nodal degrees of freedom into two arrays

$$\mathbf{d}_u = \left[u_1^1, \ldots, u_{n_d}^1, \ldots, u_1^{\bar{\mathcal{N}}_u}, \ldots, u_{n_d}^{\bar{\mathcal{N}}_u}\right]^T \tag{43}$$

$$\mathbf{d}_\chi = \left[{}^{\chi}\phi_1^1, \ldots, {}^{\chi}\phi_{n_c}^1, \ldots, {}^{\chi}\phi_1^{\bar{\mathcal{N}}_\chi}, \ldots, {}^{\chi}\phi_{n_c}^{\bar{\mathcal{N}}_\chi}\right]^T \tag{44}$$

where the subscript refers to the component of the field, and n_d is a number of dimensions of the physical space. The superscript refers to the node number, while $\bar{\mathcal{N}}_u$ and $\bar{\mathcal{N}}_\chi$ denote number of nodes with displacement and micromorphic degrees of freedom. Subscript n_c is a number of components of the micromorphic tensor ${}^{\chi}\underset{\sim}{\boldsymbol{\phi}}$ which depends on the selected type of micromorphic continua as well as on the dimension of the physical space. It is, for example, equal to three for Cosserat continuum in 3D, one for Cosserat continuum in 2D, and one for microdilatation continuum independently of the dimension of the physical space. Moreover, the micromorphic tensor ${}^{\chi}\underset{\sim}{\boldsymbol{\phi}}$ is assembled into a vector form which for the general case of full micromorphic continuum in 3D reads

$$\boldsymbol{\Xi} = \left[{}^{\chi}\phi_{11}\ {}^{\chi}\phi_{22}\ {}^{\chi}\phi_{33}\ {}^{\chi}\phi_{23}\ {}^{\chi}\phi_{13}\ {}^{\chi}\phi_{12}\ {}^{\chi}\phi_{32}\ {}^{\chi}\phi_{31}\ {}^{\chi}\phi_{21}\right]^T \tag{45}$$

Moreover, number of displacement and micromorphic degrees of freedom $\mathcal{N}_u$ and $\mathcal{N}_\chi$ can be expressed as

$$\mathcal{N}_u = n_d \bar{\mathcal{N}}_u \qquad \mathcal{N}_\chi = n_c \bar{\mathcal{N}}_\chi \tag{46}$$

The finite element approximation of displacements $\mathbf{u}$ and micromorphic vector $\boldsymbol{\Xi}$ can be expressed as

$$u_i(\mathbf{x}) \approx (u_0)_i + \sum_{I=1}^{\bar{\mathcal{N}}_u} \eta_I(\mathbf{x})(d_u)_{i+(I-1)n_d} = (\mathbf{u}_0 + \mathbf{N}_u(\mathbf{x})\mathbf{d}_u)_i \quad \forall i = 1 \ldots n_d \tag{47}$$

$$\Xi_i(\mathbf{x}) \approx (\Xi_0)_i + \sum_{I=1}^{\bar{\mathcal{N}}_\chi} \xi_I(\mathbf{x})(d_\chi)_{i+(I-1)n_c} = (\boldsymbol{\Xi}_0 + \mathbf{N}_\chi(\mathbf{x})\mathbf{d}_\chi)_i \quad \forall i = 1 \ldots n_c \tag{48}$$

where $\mathbf{N}_u$ and $\mathbf{N}_\chi$ are matrices collecting displacement and micromorphic shape functions, $\mathbf{u}_0$ and $\boldsymbol{\Xi}_0$ are chosen such that they fulfill appropriate non-homogeneous Dirichlet boundary conditions on Γ_u and Γ_χ. Applying the gradient operator to the finite element approximations gives

$$\nabla \mathbf{u}(\mathbf{x}) \approx \mathbf{B}_u(\mathbf{x})\mathbf{d}_u \tag{49}$$

$$\nabla \boldsymbol{\Xi}(\mathbf{x}) \approx \mathbf{B}_\chi(\mathbf{x})\mathbf{d}_\chi \tag{50}$$

where $\mathbf{B}_u$ and $\mathbf{B}_\chi$ are matrices containing derivatives of the shape functions and represent discrete gradient operators, that is, multiplication of the matrix with vector of nodal degrees of freedom of particular field gives an array of gradient of the field.

Substituting the finite element approximation (47)–(50) into the principle of virtual power, its discrete form is obtained

$$\begin{aligned}(\mathbf{d}_u^*)^T &\left[\int_V \mathbf{B}_u^T\boldsymbol{\sigma} - \mathbf{N}_u^T\mathbf{b}\,dV - \int_{\partial\Gamma_\sigma} \mathbf{N}_u^T\mathbf{t}_\sigma\,d\Gamma\right] \\ &+ (\mathbf{d}_\chi^*)^T\left[\int_V \mathbf{N}_\chi^T\mathbf{S} + \mathbf{B}_\chi^T\mathbf{M}\,dV - \int_{\partial\Gamma_M} \mathbf{N}_\chi^T\mathbf{t}_M\,d\Gamma\right] \\ &= 0 \quad \forall \mathbf{d}_u^*, \mathbf{d}_\chi^*\end{aligned} \tag{51}$$

where the so-called Bubnov–Galerkin formulation was used, i.e., the discretization of virtual fields and the corresponding gradients of virtual fields has the same form as approximation of the trial fields.

Equation (51) is satisfied for any virtual fields if and only if

$$\mathbf{f}_{int}(\mathbf{d}_u, \mathbf{d}_\phi) = \mathbf{f}_{ext} \tag{52}$$

$$\mathbf{g}_{int}(\mathbf{d}_u, \mathbf{d}_\phi) = \mathbf{g}_{ext} \tag{53}$$

where

$$\mathbf{f}_{int} = \int_V \mathbf{B}_u^T\boldsymbol{\sigma}\,dV, \quad \mathbf{g}_{int} = \int_V \mathbf{B}_\chi^T\mathbf{M} + \mathbf{N}_\chi^T\mathbf{S}\,dV$$

$$\mathbf{f}_{ext} = \int_V \mathbf{N}_u^T\mathbf{b}\,dV + \int_{\partial\Gamma_\sigma} \mathbf{N}_u^T\mathbf{t}_\sigma\,d\Gamma, \quad \mathbf{g}_{ext} = \int_{\partial\Gamma_M} \mathbf{N}_\chi^T\mathbf{t}_M\,d\Gamma$$

In the case of generalized linear elasticity, Eqs. (52) and (53) can be rewritten in the standard form:

$$\mathbf{K}\mathbf{d} = \mathbf{h}_{ext} \tag{54}$$

where $\mathbf{h}_{ext}$ is a vector containing classical as well as micromorphic external forces, $\mathbf{d}$ is a vector collecting displacement and micromorphic nodal degrees of freedom, $\mathbf{d}^T = [\mathbf{d}_u^T \quad \mathbf{d}_\phi^T]$, and stiffness matrix $\mathbf{K}$ can be written as

$$\mathbf{K} = \begin{bmatrix}\mathbf{K}_{uu} & \mathbf{K}_{u\chi} \\ \mathbf{K}_{\chi u} & \mathbf{K}_{\chi\chi}\end{bmatrix} \tag{55}$$

where

$$\mathbf{K}_{uu} = \int_V \mathbf{B}_u^T\mathbf{D}_{uu}\mathbf{B}_u\,dV, \quad \mathbf{K}_{u\chi} = \int_V \mathbf{B}_u^T\mathbf{D}_{u\chi}\mathbf{N}_\chi\,dV \tag{56}$$

$$\mathbf{K}_{\chi u} = \int_V \mathbf{N}_\chi^T\mathbf{D}_{u\chi}^T\mathbf{B}\,dV,$$

$$\mathbf{K}_{\chi\chi} = \int_V \left(H_\chi\mathbf{N}_\chi^T\mathbf{N}_\chi + A_\chi\mathbf{B}_\chi^T\mathbf{B}_\chi\right)dV \tag{57}$$

To finish the formulation, the constitutive matrices need to be specified. For microdilatation continuum they can be expressed as

$$\mathbf{D}_{uu} = \mathbf{E} + H_\chi \mathbf{1}\mathbf{1}^T \quad \mathbf{D}_{u\chi} = -H_\chi \mathbf{1} \tag{58}$$

and for Cosserat continuum as:

$$\mathbf{D}_{uu} = \mathbf{E} + H_\chi \mathbf{I}_{skew} \quad \mathbf{D}_{u\chi} = -H_\chi \boldsymbol{\epsilon} \tag{59}$$

where $\mathbf{E}$ is a matrix form of the stiffness matrix, $\mathbf{1}$ is a vector form of the second order unit tensor, $\mathbf{I}_{skew}$ is a matrix form of the fourth-order skew-symmetric projection tensor, and $\boldsymbol{\epsilon}$ is a matrix form of the permutation tensor.

3 Reduced order modeling

Micromorphic continua aim to model complex mechanical phenomena by introducing additional degrees of freedom for the sake of describing refined kinematics. Moreover, the micromorphic framework leads to additional balance equations with new material parameters which need to be determined. Therefore, micromorphic continua result in computationally expensive problems. Reduced-order models (ROM) are very useful to model complex mechanical problems when parametric studies are needed to estimate acceptable ranges of material constants. Typically, the quantities of interest are certain particular fields such as displacements, stresses, or micromorphic fields in our specific situation, called outputs. These fields depend on some inputs, i.e., variables such as material parameters, geometry of the problem, or loading. The connection between the output and the input is given by the partial differential equations (4) and (5). Restricting to the material parameter dependence, these equations can be rewritten in a parametrized form as

$$\operatorname{div} \underset{\sim}{\boldsymbol{\sigma}}(\boldsymbol{\mu}) + \underline{\boldsymbol{b}} = \underline{\mathbf{0}} \tag{60}$$

$$\operatorname{div} \underset{\sim}{\boldsymbol{M}}(\boldsymbol{\mu}) - \underset{\sim}{\boldsymbol{S}}(\boldsymbol{\mu}) = \underset{\sim}{\mathbf{0}} \tag{61}$$

where $\boldsymbol{\mu}$ is a vector of material parameters which may for example contain Young modulus, Poisson ratio, or internal length.

The Proper orthogonal decomposition has been widely used to construct reduced-bases for parameter-dependent partial differential equations. The key idea of the POD is to reduce the number of independent variables by projecting a finite element space into a reduced lower-dimensional space. The method of snapshots is used to obtained the reduced space, see [21].

However, the size of the basis of the reduced space has no influence on the integration of constitutive equations which can be computationally very demanding. For this reason, hyper-reduction has been proposed in [7]. In this method, a reduced integration domain (RID) is selected, so that the integration of constitutive equations is performed over just a few finite elements. On the one hand this technique saves computational time but on the other hand it leads to a greater error of the reduced model.

3.1 Proper orthogonal decomposition

The POD is a projection method that builds a basis of a subspace of a finite element space from snapshots related to an evaluation of the problem with various sets of parameters such as material coefficients or boundary conditions, that is, with different parameters contained in $\boldsymbol{\mu}$.

The POD reduction method consists in using a set of m previously computed solutions of the original problem to build a snapshot matrix:

$$\mathbf{Q} = \left[\begin{bmatrix} \mathbf{d}_u^1 \\ l_N \mathbf{d}_\chi^1 \end{bmatrix} \cdots \begin{bmatrix} \mathbf{d}_u^N \\ l_N \mathbf{d}_\chi^N \end{bmatrix} \right] \tag{62}$$

where $[(\mathbf{d}_u^i)\,(l_N \mathbf{d}_\chi^i)]^T$ denotes a predicted solution computed in ith sampling point in the parametric space and l_N is a parameter with dimension of length to scale the micromorphic degrees of freedom to the same units as displacements. Its value could be chosen so that all variables have the same order of magnitude to improve matrix conditioning. This is not essential in the present linear context but would be helpful when using iterative solvers. Nonetheless, setting of this parameter is tricky. Therefore an approach with no special treatment of micromorphic degrees of freedom, used for example in [11], is preferred. It can be obtained from (62) simply by letting $l_N = 1$ mm. A different approach to handle micromorphic degrees of freedom, based on the separate basis, is described later. Note that the number of snapshots is usually much smaller than the number of micromorphic variables as well as classical degrees of freedom.

Applying singular value decomposition to the matrix $\mathbf{Q}$, left and right singular vectors $\mathbf{V}$ and $\mathbf{U}$ and a diagonal matrix containing singular values Σ are obtained:

$$\mathbf{Q} = \mathbf{V}\Sigma\mathbf{U}^T + \mathbf{R} \tag{63}$$

Matrix $\mathbf{V}$ can be decomposed into two parts, the first one corresponding to the displacements and the second one to the micrmorphic degrees of freedom:

$$\mathbf{V} = \begin{bmatrix} \mathbf{V}_u \\ \mathbf{V}_\chi \end{bmatrix} \tag{64}$$

where the modes associated with small singular values are discarded, therefore, the number of columns of $\mathbf{V}$, denoted

by N is smaller or equal to the number of snapshots m. It is the minimal integer such that

$$||\mathbf{R}|| < \varepsilon_{tol}||\mathbf{Q}|| \tag{65}$$

where

$$||\mathbf{Q}||^2 = \sum_{i=1}^{m} \Sigma_{ii}^2 \qquad ||\mathbf{R}||^2 = \sum_{i=N+1}^{m} \Sigma_{ii}^2 \tag{66}$$

and ε_{tol} is a prescribed tolerance. Note that various norms have been proposed in the literature for the computation of POD modes, see for instance [22]. When considering a quadratic free energy to setup the constitutive equations, convenient physically-based norms can be introduced for the POD. However, in such situations, attention must be paid to define a norm that is not parameter dependent. Here, for the sake of simplicity, the Frobenius norm is used.

A few basis vectors $\boldsymbol{\psi} = \begin{bmatrix}\boldsymbol{\psi}_u & \boldsymbol{\psi}_\chi\end{bmatrix}^T$ spanning a space of small dimension are extracted using the left eigenmodes $\mathbf{V}$ and the finite element interpolations are used to approximate the variables between the sampling points

$$\boldsymbol{\psi}_k^u(\mathbf{x}) = \mathbf{N}_u(\mathbf{x})\mathbf{v}_k^u, \quad k = 1, \ldots, N \tag{67}$$
$$\boldsymbol{\psi}_k^\chi(\mathbf{x}) = \mathbf{N}_\chi(\mathbf{x})\mathbf{v}_k^\chi, \quad k = 1, \ldots, N \tag{68}$$

where $\mathbf{v}_k^u$ and $\mathbf{v}_k^\chi$ are the k^{th} columns of the matrix $\mathbf{V}^u$ and $\mathbf{V}^\chi$ respectively. These basis vectors are used to approximate the displacement and micromorphic fields

$$\begin{aligned}\mathbf{u}_{ROM}(\mathbf{x},\boldsymbol{\mu}) &= \mathbf{u}_0 + \sum_{i=1}^{N} \boldsymbol{\psi}_i^u(\mathbf{x})\gamma_i(\boldsymbol{\mu}) \\ &= \mathbf{u}_0 + \mathbf{N}_u(\mathbf{x})\mathbf{V}_u\boldsymbol{\gamma}(\boldsymbol{\mu})\end{aligned} \tag{69}$$

$$\begin{aligned}\boldsymbol{\Xi}_{ROM}(\mathbf{x},\boldsymbol{\mu}) &= \boldsymbol{\Xi}_0 + \sum_{i=1}^{N} \boldsymbol{\psi}_i^\chi(\mathbf{x})\gamma_i(\boldsymbol{\mu}) \\ &= \boldsymbol{\Xi}_0 + \mathbf{N}_\chi(\mathbf{x})\mathbf{V}_\chi\boldsymbol{\gamma}(\boldsymbol{\mu})\end{aligned} \tag{70}$$

The dependence of $\boldsymbol{\psi}$ on $\mathbf{x}$ and $\boldsymbol{\gamma}$ on $\boldsymbol{\mu}$ is for simplicity not explicitly written in the following text.

Equations (69)–(70) can be rewritten in the form

$$\mathbf{a}_{ROM} \approx \mathbf{a}_0 + \sum_{i=1}^{N} \boldsymbol{\psi}_i\gamma_i = \mathbf{a}_0 + \mathbf{N}\mathbf{V}\boldsymbol{\gamma} \tag{71}$$

where $\mathbf{a}_{ROM} = [\mathbf{u}_{ROM} \quad \boldsymbol{\Xi}_{ROM}]^T$ and $\mathbf{N}$ assembles displacement and micromorphic shape functions.

Finally, using the reduced basis approximation, the equilibrium equation (54) is transformed into

$$\mathbf{V}^T K \mathbf{V}\,\gamma = \mathbf{V}^T\mathbf{h}_{ext} \tag{72}$$

Another technique to create the reduced basis can be based on the separate basis approach, see for example [23] or [24]. In this formulation, the displacement and micromorphic degrees of freedom are collected separately into two snapshot matrices $\mathbf{Q}_u$ and $\mathbf{Q}_\chi$. Accordingly, SVD is applied separately to $\mathbf{Q}_u$ and $\mathbf{Q}_\chi$:

$$\mathbf{Q}_u = \mathbf{V}_u\Sigma_u\mathbf{U}_u^T + \mathbf{R}_u \qquad \mathbf{Q}_\chi = \mathbf{V}_\chi\Sigma_\chi\mathbf{U}_\chi^T + \mathbf{R}_\chi \tag{73}$$

Like in the previous case, the number of columns of $\mathbf{V}_u$ and $\mathbf{V}_\chi$ are denoted as N_u and N_χ. They are the minimal integers such that

$$||\mathbf{R}_u|| < \varepsilon_{tol}^u||\mathbf{Q}_u|| \qquad ||\mathbf{R}_\chi|| < \varepsilon_{tol}^\chi||\mathbf{Q}_\chi|| \tag{74}$$

where

$$||\mathbf{Q}_u||^2 = \sum_{i=1}^{m}(\Sigma_{ii}^u)^2 \qquad ||\mathbf{R}_u||^2 = \sum_{i=N_u+1}^{m}(\Sigma_{ii}^u)^2 \tag{75}$$

and

$$||\mathbf{Q}_\chi||^2 = \sum_{i=1}^{m}(\Sigma_{ii}^\chi)^2 \qquad ||\mathbf{R}_\chi||^2 = \sum_{i=N_\chi+1}^{m}(\Sigma_{ii}^\chi)^2 \tag{76}$$

Moreover, ε_{tol}^u and ε_{tol}^χ are prescribed tolerances.

A few basis vectors $\boldsymbol{\psi}_u$ and $\boldsymbol{\psi}_\chi$ spanning a space of small dimension are extracted using the matrix of left singular vectors $\mathbf{V}$ which is assembled as

$$\mathbf{V} = \begin{bmatrix}\mathbf{V}_u & \mathbf{0} \\ \mathbf{0} & \mathbf{V}_\chi\end{bmatrix} \tag{77}$$

3.2 Hyper-reduction

In order to improve computational efficiency of the POD-reduced model, the hyper-reduction method is used. In this method, the equilibrium equations are assembled only over a subdomain, called reduced integration domain (RID) and denoted by Ω_Λ. The construction of the RID follows a heuristic reasoning: if the RID enables the interpolation of degrees of freedom and the interpolation of stresses by using dedicated POD reduced bases, then it should be convenient to set up the hyper-reduced equilibrium equations. Here, the RID aggregates the elements containing interpolation points generated by the Discrete Empirical Interpolation Method (DEIM), see [25].

Given $\mathbf{V}$, the DEIM selects N rows of $\mathbf{V}$ by introducing a selection matrix $\mathbf{P} \in \mathbb{R}^{(\mathcal{N}_u+\mathcal{N}_\chi)\times N}$ such that $\mathbf{P}^T\mathbf{V}$ is invertible. Each column of $\mathbf{P}$ has a unique nonzero entry, equal to one, that selects a value to interpolate. Since $\mathbf{V}$ is generated by finite element simulations, the values selected by $\mathbf{P}^T\mathbf{V}$ are located at the nodes of the mesh. All the elements

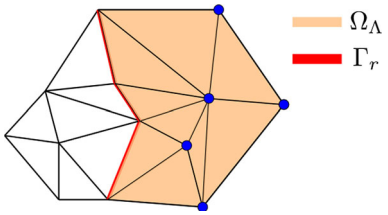

Fig. 1 Reduced integration domain Ω_Λ. The blue nodes are the interpolation points selected by the DEIM. The *red line* represents the interface Γ_r between the original mesh and the RID. (Color figure online)

connected to these nodes are incorporated in the RID. A similar approach is applied separately on the Cauchy stress $\underset{\sim}{\boldsymbol{\sigma}}$ as well as the higher order stress $\underset{\approx}{\boldsymbol{M}}$. The related snapshots are local average stresses evaluated at the nodes of the mesh. For instance, the average nodal stresses at node number I read :

$$\frac{1}{\int_\Omega I(\eta_I)\,dV}\int_\Omega I(\eta_I)\underset{\sim}{\boldsymbol{\sigma}}\,dV \quad \text{and} \quad \frac{1}{\int_\Omega I(\eta_I)\,dV}\int_\Omega I(\eta_I)\underset{\approx}{\boldsymbol{M}}\,dV \tag{78}$$

where $I(\eta_I)$ is the indicator function of the shape function η_I. Then the POD followed by the DEIM generate two selection matrices $\mathbf{P}^\sigma$ and $\mathbf{P}^M$, where the selected interpolation entries are also attached to the nodes of the mesh. All the elements of the mesh connected to these entries are also added to the RID. The user of the method can also add a zone of interest to the RID. By construction, the RID has an interface, denoted by Γ_r, without given boundary condition, see Fig. 1. This interface reads:

$$\Gamma_r = \Omega_\Lambda \cap \overline{\Omega\backslash\Omega_\Lambda} \tag{79}$$

where $\overline{\Omega\backslash\Omega_\Lambda}$ includes the boundary of $\Omega\backslash\Omega_\Lambda$. The hyper-reduction method aims at imposing Dirichlet boundary conditions on Γ_r, such that:

$$\mathbf{u}_{HR} = \mathbf{u}_{\Gamma_r} \quad \forall \mathbf{x} \in \Gamma_r \tag{80}$$
$$\Xi_{HR} = \Xi_{\Gamma_r} \quad \forall \mathbf{x} \in \Gamma_r \tag{81}$$

where $\mathbf{u}_{\Gamma_r}$ and Ξ_{Γ_r} are finite element fields that are set to zero in Ω_Λ, except for the nodes on Γ_r. These boundary conditions are expressed as a linear combination of N modes extracted from the reduced basis $(\boldsymbol{\psi}_k)_{k=1}^N$. These modes are denoted by $\boldsymbol{\psi}_k^\delta$. The first step to specify the boundary conditions on Γ_r is the splitting of each empirical mode $\boldsymbol{\psi}_k$ into two parts denoted by $\boldsymbol{\psi}_k^\Lambda$ and $\boldsymbol{\psi}_k^\delta$. The first part $\boldsymbol{\psi}_k^\Lambda$ is related to the finite element nodes inside the RID except the interface nodes:

$$\boldsymbol{\psi}_k^{u\Lambda}(\mathbf{x}) = \mathbf{N}_u(\mathbf{x})\Lambda^u\mathbf{v}_k^u \tag{82}$$
$$\boldsymbol{\psi}_k^{\chi\Lambda}(\mathbf{x}) = \mathbf{N}_\chi(\mathbf{x})\Lambda^\chi\mathbf{v}_k^\chi \tag{83}$$

where Λ^u and Λ^χ are diagonal matrices such that:

$$\Lambda_{ii}^u = 1 \quad \text{if} \int_{\Omega\backslash\Omega_\Lambda} (\mathbf{N}_u(\mathbf{x})^T\,\mathbf{N}_u(\mathbf{x}))_{ii}\,dx = 0, \quad \text{else } \Lambda_{ii}^u = 0, \quad i = 1,\ldots\mathcal{N}_u \tag{84}$$

$$\Lambda_{ii}^\chi = 1 \quad \text{if} \int_{\Omega\backslash\Omega_\Lambda} (\mathbf{N}_\chi(\mathbf{x})^T\,\mathbf{N}_\chi(\mathbf{x}))_{ii}\,dx = 0, \quad \text{else } \Lambda_{ii}^\chi = 0, \quad i = 1,\ldots\mathcal{N}_\chi \tag{85}$$

The second part $\boldsymbol{\psi}^\delta$ is associated with the exterior of the RID and the interface, namely the remainder of the original mode $\boldsymbol{\psi}_k$:

$$\boldsymbol{\psi}_k^{u\delta} = \boldsymbol{\psi}_k^u - \boldsymbol{\psi}_k^{u\Lambda} \tag{86}$$
$$\boldsymbol{\psi}_k^{\chi\delta} = \boldsymbol{\psi}_k^\chi - \boldsymbol{\psi}_k^{\chi\Lambda} \tag{87}$$

The Dirichlet boundary condition on Γ_r is expressed by introducing additional reduced coordinates $(\tilde{\gamma}_k)_{k=1}^N$ such that:

$$\mathbf{u}_{\Gamma_r} = \sum_{k=1}^N \boldsymbol{\psi}_k^{u\delta}\tilde{\gamma}_k \tag{88}$$

$$\boldsymbol{\Xi}_{\Gamma_r} = \sum_{k=1}^N \boldsymbol{\psi}_k^{\chi\delta}\tilde{\gamma}_k \tag{89}$$

This is not an usual boundary condition because $\tilde{\boldsymbol{\gamma}}$ is not a priori known. Finally, the hyper-reduced solution in the RID can be expressed as

$$\mathbf{u}_{HR} = \mathbf{u}_0 + \mathbf{u}_{\Gamma_r} + \sum_{k=1}^N \boldsymbol{\psi}_k^{u\Lambda}\gamma_k \tag{90}$$

$$\Xi_{HR} = \Xi_0 + \Xi_{\Gamma_r} + \sum_{k=1}^N \boldsymbol{\psi}_k^{\chi\Lambda}\gamma_k \tag{91}$$

This approach defines convenient test functions for the setting of the hyper-reduced equilibrium equations over the RID. According to Eqs. (90) and (91), these test functions are $(\boldsymbol{\psi}_k^\Lambda)_{k=1}^N$ such that $\boldsymbol{\psi}_k^\Lambda = [\boldsymbol{\psi}_k^{u\Lambda}\ \boldsymbol{\psi}_k^{\chi\Lambda}]^T$. The related matrix form of these test functions is the following:

$$\sum_{k=1}^N \boldsymbol{\psi}_k^\Lambda\gamma_k^* = \begin{bmatrix}\mathbf{N}_u\Lambda^u\mathbf{V}^u\boldsymbol{\gamma}^* \\ \mathbf{N}_\chi\Lambda^\chi\mathbf{V}^\chi\boldsymbol{\gamma}^*\end{bmatrix} = \begin{bmatrix}\mathbf{N}_u \\ \mathbf{N}_\chi\end{bmatrix}\Lambda\mathbf{V}\boldsymbol{\gamma}^*, \quad \forall\boldsymbol{\gamma}^* \in \mathbb{R}^N \tag{92}$$

where $\boldsymbol{\Lambda}$ is a block-diagonal matrix. It assembles $\boldsymbol{\Lambda}^u$ and $\boldsymbol{\Lambda}^\chi$. Because of the added boundary conditions, $\boldsymbol{u}_{HR}$ and $\boldsymbol{\Xi}_{HR}$ are linear functions of the added reduced coordinates $(\tilde{\gamma}_k)_{k=1}^N$:

$$\mathbf{u}_{HR} = \mathbf{u}_0 + \mathbf{N}_u\left((\mathbf{I}^u - \Lambda^u)\,\mathbf{V}^u\tilde{\boldsymbol{\gamma}} + \Lambda^u\mathbf{V}^u\boldsymbol{\gamma}\right) \tag{93}$$
$$\Xi_{HR} = \Xi_0 + \mathbf{N}_\chi\left((\mathbf{I}^\chi - \Lambda^\chi)\,\mathbf{V}^\chi\tilde{\boldsymbol{\gamma}} + \Lambda^\chi\,\mathbf{V}^\chi\boldsymbol{\gamma}\right) \tag{94}$$

The usual reduced basis approximation is recovered by choosing the following closure equation $\tilde{\boldsymbol{\gamma}} = \boldsymbol{\gamma}$. Hence, the hyper-reduced solution reads

$$\mathbf{u}_{HR} = \mathbf{u}_0 + \mathbf{N}_u \, \mathbf{V}^u \boldsymbol{\gamma} \tag{95}$$

$$\Xi_{HR} = \Xi_0 + \mathbf{N}_\chi \, \mathbf{V}^\chi \boldsymbol{\gamma} \tag{96}$$

Substituting back to the weak form, we arrive at

$$\begin{aligned}(\boldsymbol{\gamma}^*)^T \Bigg[& \int_{\Omega_\Lambda} \mathbf{V}_u^T \Lambda_u \mathbf{B}_u^T \boldsymbol{\sigma} \\ & - \mathbf{V}_u^T \Lambda_u \mathbf{N}_u^T \mathbf{b} \, dV - \int_{\partial\Gamma} \mathbf{V}_u^T \Lambda_u \mathbf{N}_u^T \mathbf{t}_\sigma \, d\Gamma \Bigg] \\ & + (\boldsymbol{\gamma}^*)^T \Bigg[\int_{\Omega_\Lambda} \mathbf{V}_\chi^T \Lambda_\chi \mathbf{N}_\chi^T \mathbf{S} + \mathbf{V}_\chi^T \Lambda_\chi \mathbf{B}_\chi^T \mathbf{M} \, dV \\ & - \int_{\partial\Gamma} \mathbf{V}_\chi^T \Lambda_\chi \mathbf{N}_\chi^T \mathbf{t}_M \, d\Gamma \Bigg] = 0 \quad \forall \boldsymbol{\gamma}^* \in \mathbb{R}^N \end{aligned} \tag{97}$$

Thus, following equilibrium equation needs to be satisfied:

$$\mathbf{V}^T \Lambda \mathbf{K}_r \mathbf{V} \, \boldsymbol{\gamma} = \mathbf{V}^T \Lambda \mathbf{h}_r \tag{98}$$

where $\mathbf{K}_r$ and $\mathbf{h}_r$ are the classical stiffness matrix and external forces; however, they are assembled only over the RID.

3.3 A posteriori error estimator

In this section, we propose an error estimator to guess a validity domain of the hyper-reduced approximation. The selection of positions of sampling points, i.e., values of material parameters for which the snapshots are computed is complicated. Therefore, introduction of the error estimator is important to validate or adapt the choices of the sampling points. The finite element solution satisfies equilibrium equation

$$\mathbf{K}\mathbf{a} = \mathbf{h}_{ext} \tag{99}$$

As shown in [26], this equation is satisfied by the reduced order model only approximately

$$\mathbf{K}\mathbf{a}_{HROM} = \mathbf{h}_{ext} + \mathbf{r} \tag{100}$$

where $\mathbf{r}$ is the residuum which can be expressed as

$$\mathbf{r} = \mathbf{K} \, (\mathbf{a}_{HROM} - \mathbf{a}) \tag{101}$$

The proposed error-estimators for displacements and micromorphic degrees of freedom are based on the infinity norm of the residuum and read

$$\eta_u = \lambda_u(\boldsymbol{\mu}) \|\mathbf{r}\|_\infty, \quad \eta_\chi = \lambda_\chi(\boldsymbol{\mu}) \|\mathbf{r}\|_\infty \tag{102}$$

where $\lambda_u(\boldsymbol{\mu})$ and $\lambda_\chi(\boldsymbol{\mu})$ are numerical parameters which need to be also estimated. In [6], it was shown that $1/\lambda$ is equal to the Babuška inf-sup constant of the given partial differential equation, that is the minimum singular value associated with it when considering a L^2 norm. However, computation of such a constant or its approximation is complex. Therefore, we propose a heuristic approach where the constants $\lambda_u(\boldsymbol{\mu})$ and $\lambda_\chi(\boldsymbol{\mu})$ are decomposed as

$$\lambda_u(\boldsymbol{\mu}) = \frac{\alpha_u}{\beta(\boldsymbol{\mu})}, \quad \lambda_\chi(\boldsymbol{\mu}) = \frac{\alpha_\chi}{\beta(\boldsymbol{\mu})} \tag{103}$$

That is, the error estimators read

$$\eta_u = \frac{\alpha_u}{\beta(\boldsymbol{\mu})} \|\mathbf{r}\|_\infty, \quad \eta_\chi = \frac{\alpha_\chi}{\beta(\boldsymbol{\mu})} \|\mathbf{r}\|_\infty \tag{104}$$

where the evaluation of infinity norm of the residual is restricted to the RID. Furthermore, β is related to the internal length parameter of the given problem and was heuristically chosen as $\beta_i(\boldsymbol{\mu}) = \sqrt{l_i}$, see Eq. (113) in the next section for an example of l_i; α_u and α_χ are estimated numerically using an approach similar to one presented in [27]. The constants α_u and α_χ are obtained from the residuum and approximate hyper-reduced solutions related to the snapshots as

$$\alpha_u = \max_{\tilde{\mathbf{V}} \in \mathcal{V}, i \in \mathcal{I}} \frac{\beta_i(\boldsymbol{\mu}) \, ||\mathbf{u}_{FEM}(\mu_i) - \tilde{\mathbf{u}}_{HROM}(\mu_i)||}{||\tilde{\mathbf{r}}(\mu_i)||_\infty} \tag{105}$$

and

$$\alpha_\chi = \max_{\tilde{\mathbf{V}} \in \mathcal{V}, i \in \mathcal{I}} \frac{\beta_i(\boldsymbol{\mu} \, ||\chi_{FEM}(\mu_i) - \tilde{\chi}_{HROM}(\mu_i)||}{||\tilde{\mathbf{r}}(\mu_i)||_\infty} \tag{106}$$

where $\tilde{\mathbf{u}}_{HROM}$ and $\tilde{\chi}_{HROM}$ denote hyper-reduced solutions obtained using the reduced basis matrix $\tilde{\mathbf{V}}$ and $\tilde{\mathbf{r}}$ is the associated residuum. The reduced basis matrix $\tilde{\mathbf{V}}$ is set-up by restricting the number of available modes, and a set of reduced basis matrices $\mathcal{V}$ is generated ranging from a reduced basis matrix containing only one mode up to the reduced basis matrix consisting of all modes N. In addition, $\mathcal{I}$ denotes a set of all snapshots.

4 Numerical examples

To investigate the performance of the hyper-reduction, three numerical simulations have been carried out. The POD, hyper-reduction, and micromorphic continua were implemented into OOFEM [28,29], an object-oriented finite element code. Note that the structure of the finite element formulation of micromorphic continua fits into the framework presented in [30].

4.1 Simple extension test for the microdilatation continua

First, a simple illustrative example of uni-axial extension of a microdilatation elastic bar is assumed. Uni-axial extension leads to a one-dimensional problem which keeps the analysis simple and can be solved analytically. We look for a displacement field in the form

$$u_x = u(x), \quad u_y = 0, \quad u_z = 0 \tag{107}$$

The equilibrium equations (4) and (5) combined with constitutive equations (22), (23), and (24) reduce to

$$(\lambda + 2\mu + H_\chi)u'' - H_\chi \chi' = 0 \tag{108}$$
$$A_\chi \chi'' - H_\chi(\chi' - u') = 0 \tag{109}$$

where the prime denotes differentiation with respect to the spatial variable x. The problem is described by kinematic boundary conditions

$$u(0) = 0 \quad u(L) = \bar{u} \tag{110}$$
$$\chi(0) = 0 \quad \chi(L) = 0 \tag{111}$$

where L is the length of the bar and $\bar{u}$ is a prescribed displacement at the right edge of the bar.

It is worth noting that the physical meaning of constraining micromorphic degrees of freedom is a difficult topic that depends on the specific physical content of the model. The boundary conditions for the micromorphic degrees of freedom are briefly discussed at the end of this section.

Substituting derivative of Eq. (109) with respect to x into (108) and after some rearrangement we get

$$\chi''' - \frac{1}{l_e^2}\chi' = 0 \tag{112}$$

where l_e is the internal length parameter for the uni-axial extension problem defined as

$$l_e^2 = \frac{(\lambda + 2\mu + H_\chi)A_\chi}{(\lambda + 2\mu)H_\chi} = \frac{A_\chi}{H_\chi} + \frac{A_\chi}{\lambda + 2\mu} \tag{113}$$

The above differential equation has a general solution

$$\chi = C_1 \sinh\left(\frac{x}{l_e}\right) + C_2 \cosh\left(\frac{x}{l_e}\right) + C_3 \tag{114}$$

where C_1, C_2, and C_3 are integration constants which are determined such that the solution satisfies the equilibrium equation (108) and the boundary conditions (111):

$$C_1 = -\frac{H_\chi}{(\lambda + 2\mu + H_\chi)L}\bar{u},$$
$$C_2 = \frac{\sinh\frac{L}{l_e}}{1 - \cosh\frac{L}{l_e}}C_1, \quad C_3 = -C_2 \tag{115}$$

Combining (114) with (108) provides the expression for the displacement field

$$u = K_1 \cosh\left(\frac{x}{l_e}\right) + K_2 \sinh\left(\frac{x}{l_e}\right) + K_3 x + K_4 \tag{116}$$

The integration constants are obtained from the boundary conditions

$$K_1 = -\frac{H_\chi l_e}{\lambda + 2\mu + H_\chi}C_1,$$
$$K_2 = \frac{H_\chi l_e}{(\lambda + 2\mu + H_\chi)}C_1 \tag{117}$$
$$K_3 = \frac{\bar{u}}{L} + \frac{2H_\chi l_e}{(\lambda + 2\mu + H_\chi)L}C_1,$$
$$K_4 = -\frac{H_\chi l_e}{(\lambda + 2\mu + H_\chi)}C_1 \tag{118}$$

The obtained analytical solution can be used for the verification of the numerical implementation of microdilatation elasticity. Whatever the boundary conditions are, the solution has hyperbolic form which significantly differs from the classical homogeneous solution. Note that this type of solution is typical for all kinds of micromorphic continua and it is not of the separable type assumed by POD.

In the finite element simulation, the length of the bar was $L = 2$ mm and the height of the bar was $h = 1$ mm. The Young modulus was chosen as 70,000 MPa, the Poisson coefficient was 0.4, $H_\chi = 10^6$ MPa and we investigated

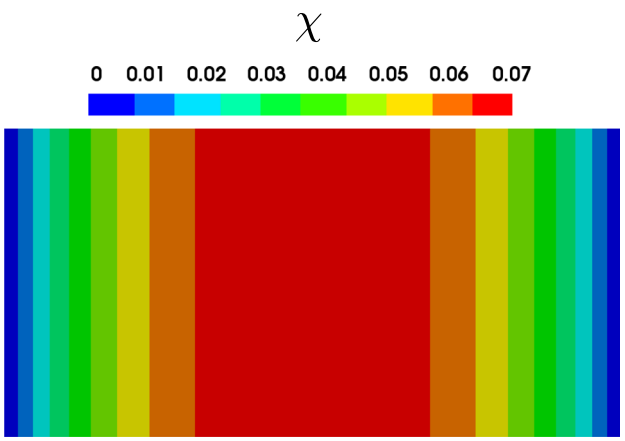

Fig. 2 Extension test: microdilatation contour plots, for $l_e = 0.5$ mm, L = 2 mm, and $\bar{u} = 0.1$ mm

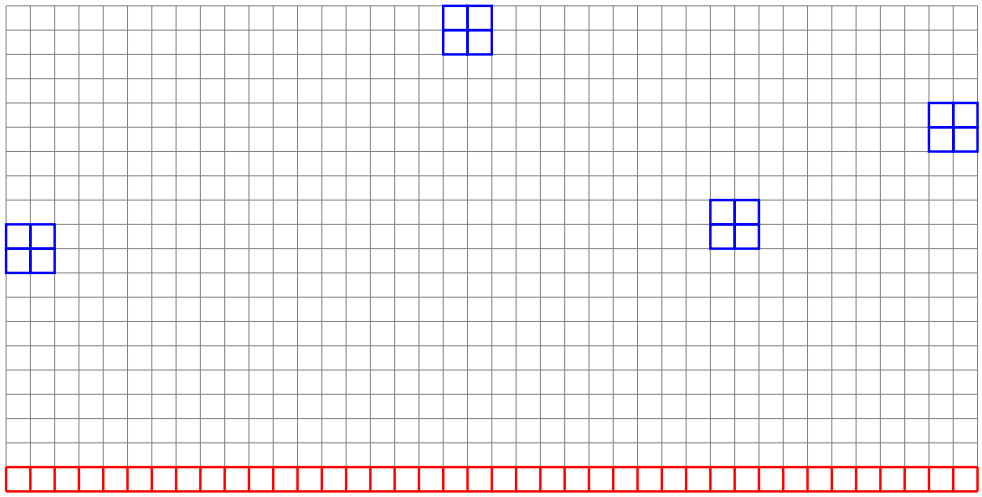

Fig. 3 Extension test: full mesh in *black*, a priory chosen RID in *red*, automatically selected RID in *blue*. (Color figure online)

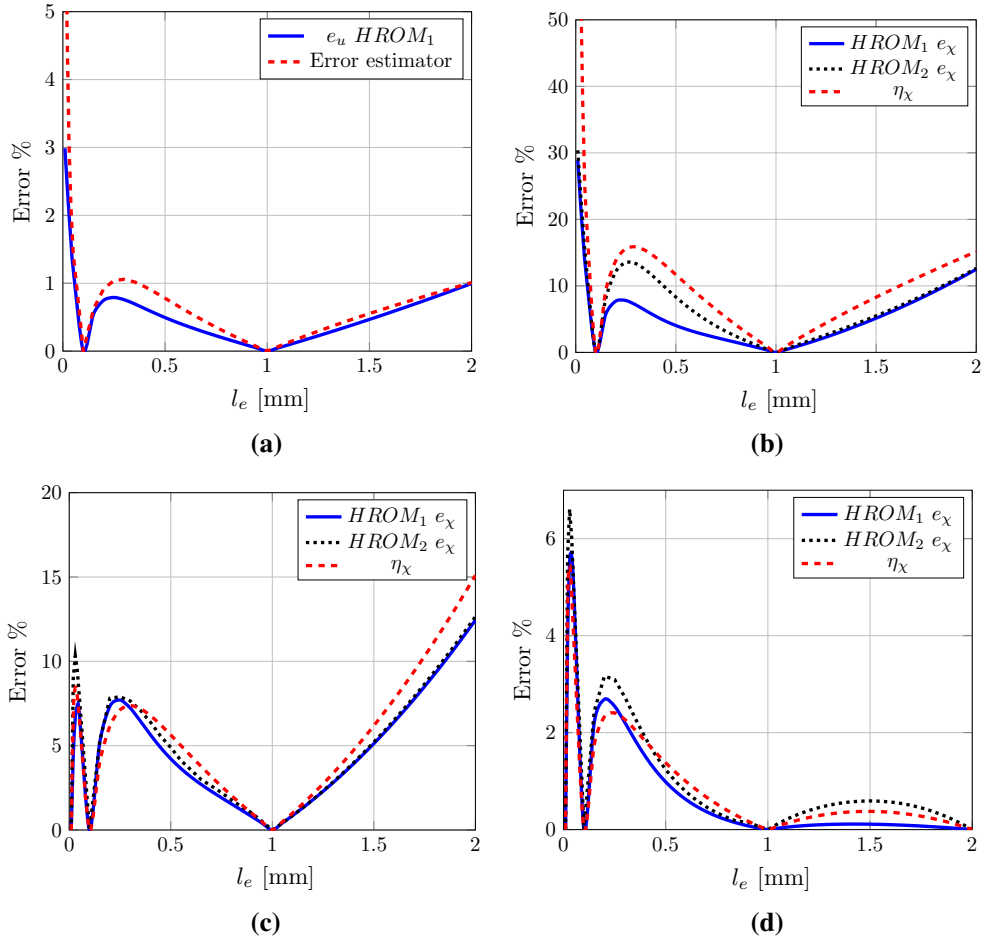

Fig. 4 Error of the hyper-reduced computation of the extension test: **a** displacement field, 2 snapshots $\mathbf{l}_s = [0.1, 1]$ mm, **b** microdilatation field, 2 snapshots $\mathbf{l}_s = [0.1, 1]$ mm, **c** microdilatation field, 3 snapshots $\mathbf{l}_s = [0.1, 0.01, 1]$ mm, **d** microdilatation field, 4 snapshots $\mathbf{l}_s = [0.1, 0.01, 1, 2]$ mm

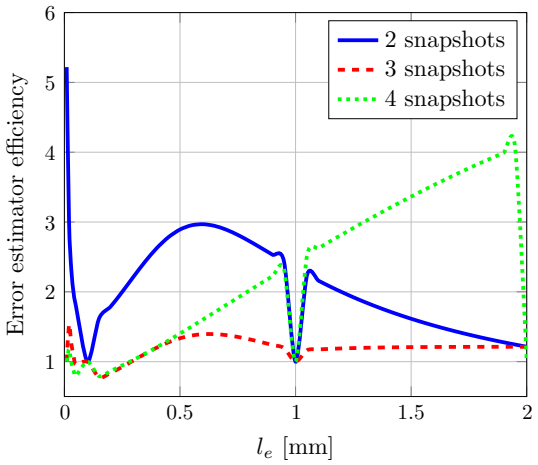

Fig. 5 Extension test: HROM_1 error estimator efficiency

the difference between the finite element and hyper-reduced solutions for different values of the internal length parameter l_e varying between 0.01 and 2 mm, i.e., $\mu = [l_e]$. The internal length parameter is linked to the parameter A_χ through Eq. (113). The example was discretized using bi-linear quadrilateral finite element shape functions for the displacement as well as for the microdilatation degree of freedom. Example of contour plots of the microdilatation field for $l_e = 0.5$ mm can be seen in Fig. 2.

To set-up the POD basis, two sampling points were arbitrary chosen as $l_e = 0.1$ mm and $l_e = 1$ mm. A vector containing snapshot parameters was $\boldsymbol{l}_s = [0.1, 1]$ mm. Differences between full finite element simulations and hyper-reduced calculations with two different RID were explored. The RID for the first case is depicted in Fig. 3 in red. It was selected a priori to validate our implementation

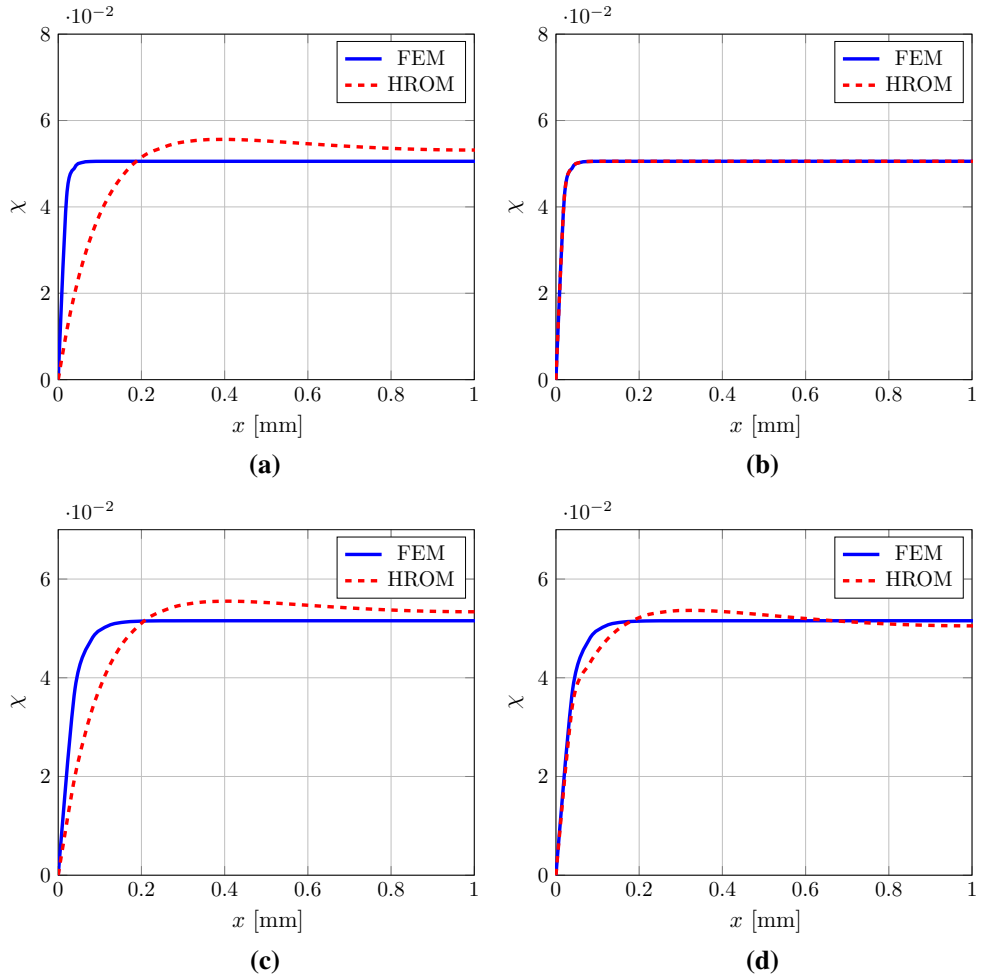

Fig. 6 Extension test: comparison of finite element and hyper-reduced solution of the distribution of the microdilatation field along the bar with L = 2 mm, $\bar{u} = 0.1$ mm: **a** $l_e = 0.01$ mm, 2 snapshots $\mathbf{l}_s = [0.1, 1]$ mm, **b** $l_e = 0.01$ mm, 4 snapshots $\mathbf{l}_s = [0.01, 0.1, 1, 2]$ mm, **c** $l_e = 0.03$ mm, 2 snapshots $\mathbf{l}_s = [0.1, 1]$ mm, **d** $l_e = 0.03$ mm, 4 snapshots $\mathbf{l}_s = [0.01, 0.1, 1, 2]$ mm. Only half of the bar is shown due to the symmetry

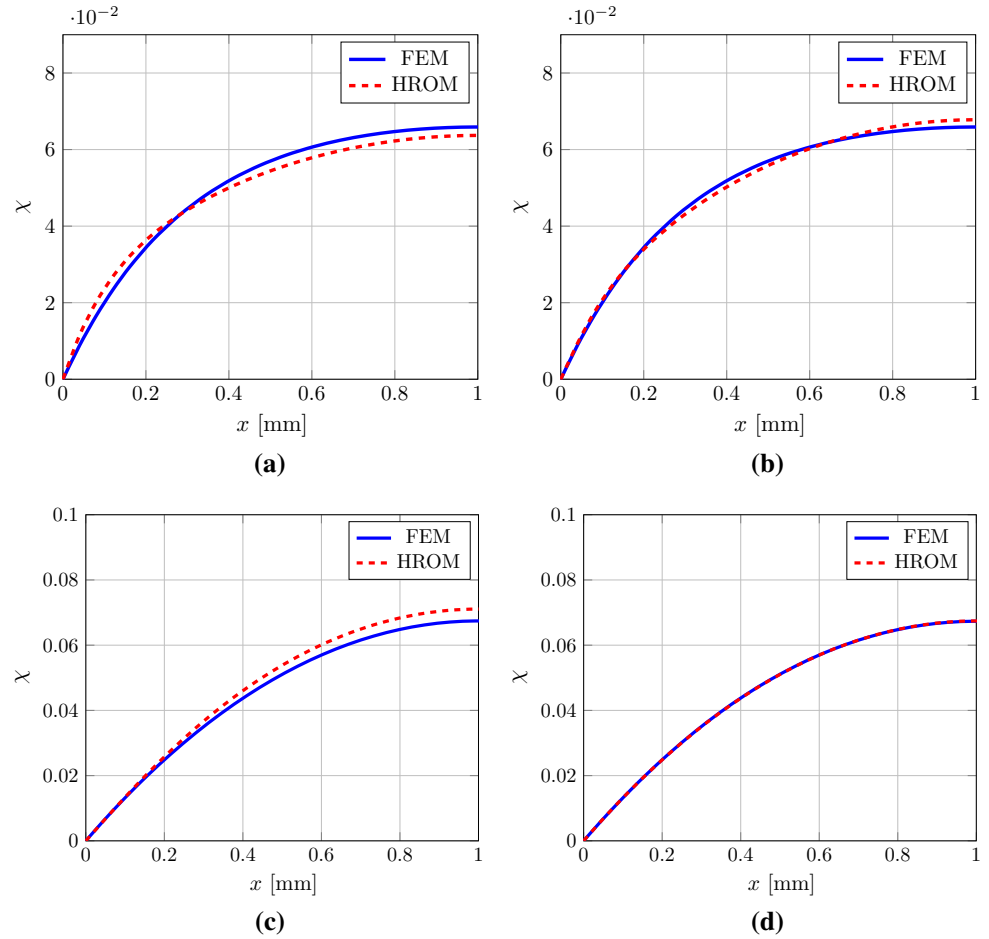

Fig. 7 Extension test: comparison of finite element and hyper-reduced solution of the distribution of the microdilatation field along the bar with L = 2 mm, $\bar{u} = 0.1$ mm: **a** $l_e = 0.3$ mm, 2 snapshots $\mathbf{l}_s = [0.1, 1]$ mm, **b** $l_e = 0.3$, 4 snapshots $\mathbf{l}_s = [0.01, 0.1, 1, 2]$ mm, **c** $l_e = 1.5$ mm, 2 snapshots $\mathbf{l}_s = [0.1, 1]$ mm, **d** $l_e = 1.5$ mm, 4 snapshots $\mathbf{l}_s = [0.01, 0.1, 1, 2]$ mm. Only half of the bar is shown due to the symmetry

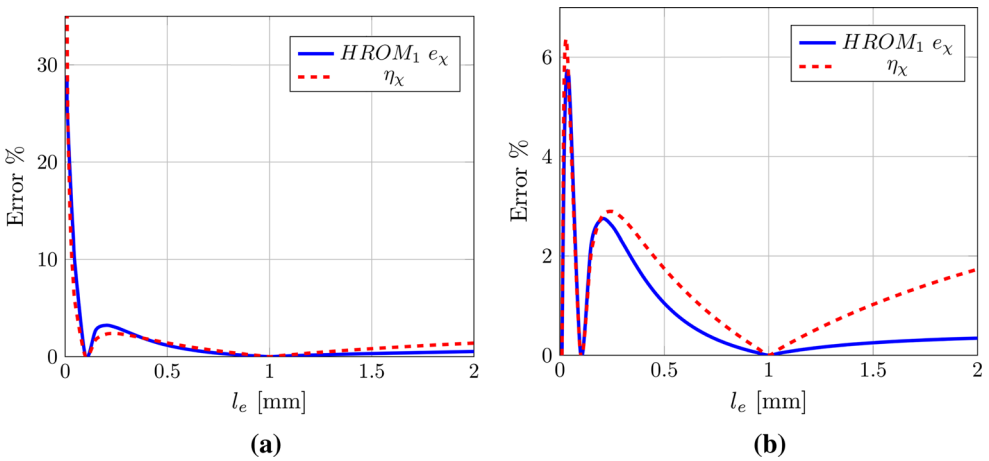

Fig. 8 Error of the hyper-reduced computation of the extension test with separate basis. Microdilatational field: **a** 2 snapshots $\mathbf{l}_s = [0.1, 1]$ mm, **b** 3 snapshots $\mathbf{l}_s = [0.01, 0.1, 1]$ mm

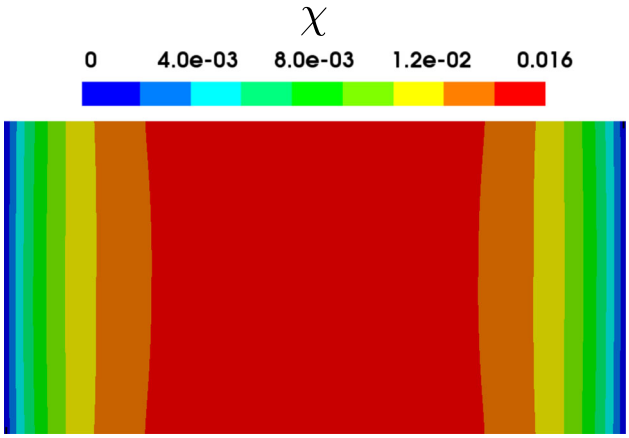

Fig. 9 Clamped tension test. Microdilatation contour plots with $l_e = 0.3$ mm, $L = 2$ mm, and $\bar{u} = 0.1$ mm

of the hyper-reduction. As the solution is one-dimensional, the hyper-reduced solution with properly extracted boundary conditions at the interface of the a priory selected RID should lead to the same solution as the POD and this assumption was satisfied. The RID for the second case was computed using the DEIM approach as described in the previous section. The RID is showed in Fig. 3 in blue. Note that a finer mesh was used in the actual simulations, but the number of elements in the RID for the second simulation remained the same. Figure 4a reproduces an error between FEM and two hyper-reduced order models (HROM) for displacement field and Fig. 4b for the microdilatation degree of freedom. The errors for the displacements and micromorphic field are defined as

$$e_u = \frac{||\mathbf{d}_{FEM} - \mathbf{d}_{HROM}||}{||\mathbf{d}_{FEM}||} \tag{119}$$

$$e_\chi = \frac{||\Xi_{FEM} - \Xi_{HROM}||}{||\Xi_{FEM}||} \tag{120}$$

The first as well as the second HROM solution obtained using two snapshots led to a low error of the displacement field; however, the highest error of the microdilatation degree of freedom is around 30%. Therefore, a new snapshot is added to the reduced basis based on the error estimator in order to improve the space where the solution is searched for. The third snapshot was selected as $l_e = 0.01$ mm. The

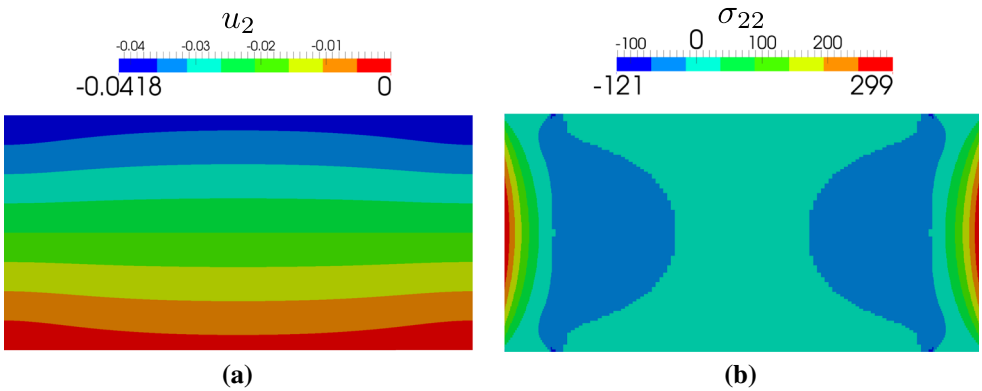

Fig. 10 Contour plots of clamped tension test with $l_e = 0.3$ mm, $L = 2$ mm, and $\bar{u} = 0.1$ mm: **a** displacement field u_2, **b** stress field σ_{22}

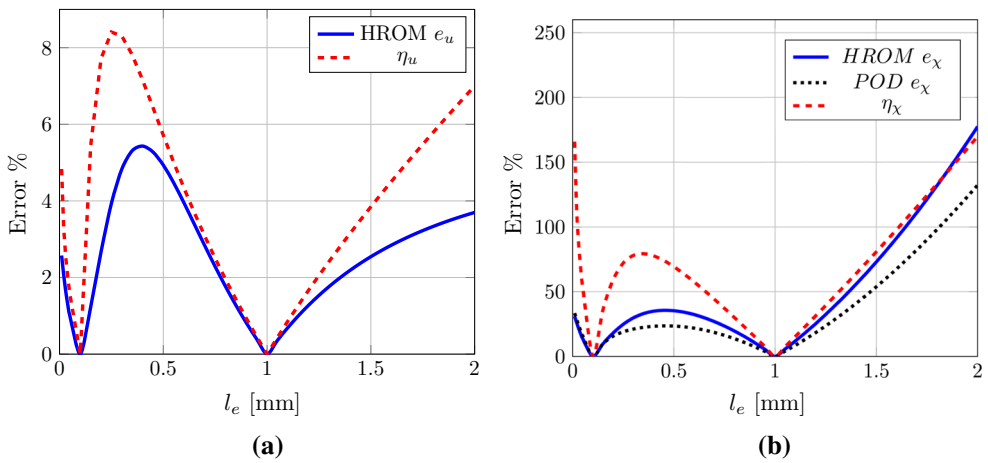

Fig. 11 Error of the hyper-reduced computation of the clamped tension test with 2 snapshots with $\mathbf{l}_s = [0.1, 1]$ mm: **a** displacement field, **b** microdilatation field

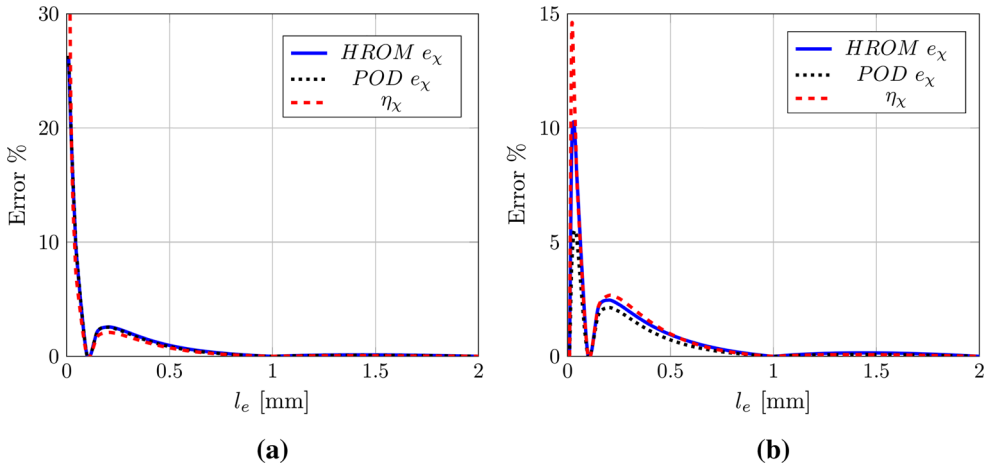

Fig. 12 Clamped tension test: error of the hyper-reduced solution of the microdilatation field with: **a** 3 snapshots, $\mathbf{l}_s = [0.1, 1, 2]$ mm, **b** 4 snapshots, $\mathbf{l}_s = [0.01, 0.1, 1, 2]$ mm

errors together with the error estimator for this case can be seen in Fig. 4c. The procedure was repeated once more and the new sampling point $l_e = 2$ mm was selected. These simulations lead to errors below 7% in the whole domain, see Fig. 4d. It is worth noting that this procedure can be repeated until the error is everywhere below a certain prescribed tolerance. This procedure is similar to the greedy algorithms proposed in [5,26]. Moreover, Fig. 5 shows the efficiency of the estimator for the micromorphic degrees of freedom, i.e., the ratio between the error estimator and the true error e_χ for the first HROM simulation. It is important to note that the dimension of the reduced basis coincide with the number of snapshots, because all of them are relevant in the present computations; therefore, no modes were discarded.

Figures 6 and 7 illustrate the distribution of the microdilatation field along the bar for different values of the internal length parameter. Only results of the hyper-reduced model with the a priory chosen RID are presented. The left column is related to simulations with two snapshots while the results in the right column were obtained with four snapshots. Obviously, the field is varying along the bar for two snapshots, while very good match can be observed for four snapshots.

Next, the investigation of the reduced-order modeling of microdilatation extension was repeated using the separate basis approach for the first hyper-reduced order model, i.e., for the model with the a priory chosen RID. The reduced order model was again set-up using the same two sampling points, that is, $l_e = 0.1$ mm and $l_e = 1$ mm. Relatively high error of the microdilatation field can be observed in Fig. 8a, mainly for small values of the internal length. Therefore, a third snapshot, $l_e = 0.01$ mm, was added to the reduced basis leading to relatively low error in the whole domain, see Fig. 8b.

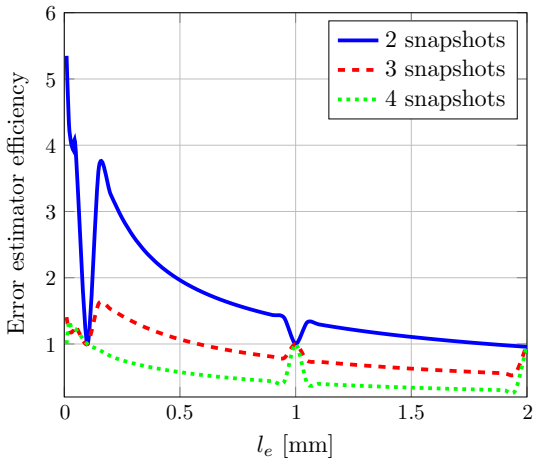

Fig. 13 Clamped tension test: error estimator efficiency

4.2 Clamped tension test of microdilatation continuum

The previous example led to accurate results; nevertheless, it was only a 1D problem. To demonstrate the potential of the hyper-reduction in a more general case, a clamped tension test was performed. The boundary conditions were taken from the extension case:

$$u_x(0, y) = 0 \quad u_x(L, y) = \bar{u} \quad u_y(0, 0) = 0 \tag{121}$$

$$\chi(0, y) = 0 \quad \chi(L, y) = 0 \tag{122}$$

However, u_y is fixed just in one point and the solution is not anymore one-dimensional, see Fig. 9 for the microdilatation contour plots. To highlight the 2D character of the solution, contour plots of horizontal displacement u_2 and stress σ_{22} are shown in Fig. 10.

The geometry and material properties were adopted from the previous case, $L = 2$ mm, $h = 1$ mm, $E = 70{,}000$ MPa,

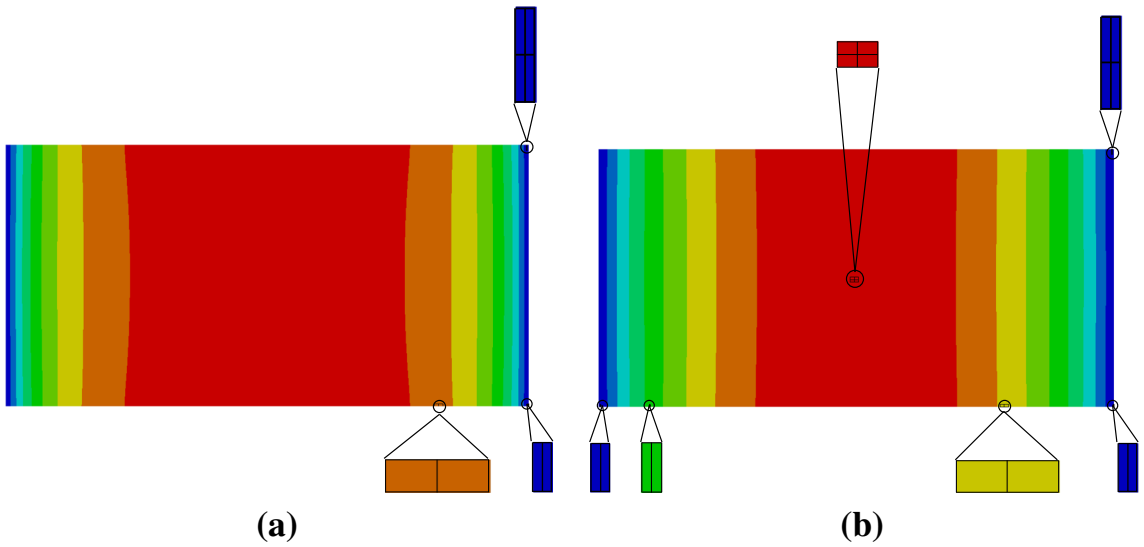

Fig. 14 Clamped tension test: reduced integration domain generated by DEIM, **a** 2 snapshots, **b** 4 snapshots

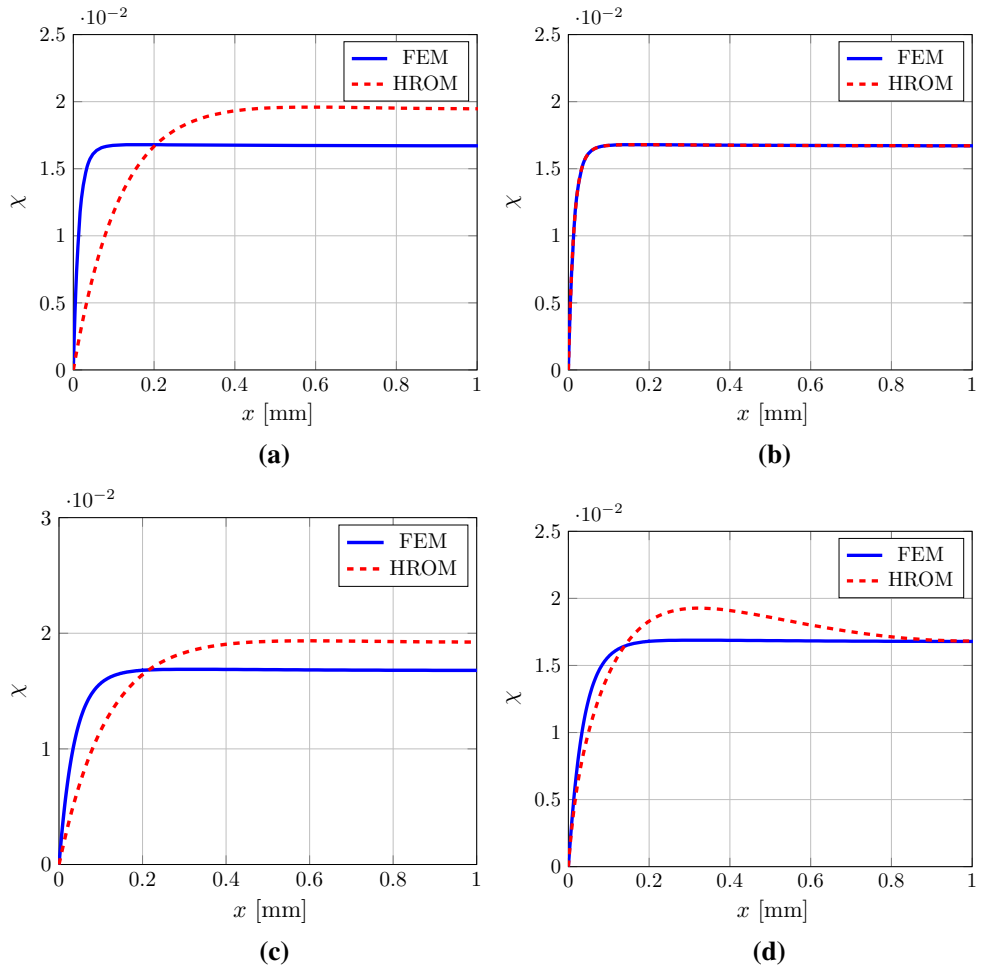

Fig. 15 Clamped tension test: comparison of finite element and hyper-reduced solution of the distribution of the microdilatation field along the x-direction in the middle of the height of the bar with L = 2 mm, $\bar{u} = 0.1$ mm: **a** $l_e = 0.01$ mm, 2 snapshots, $\mathbf{l}_s = [0.1, 1]$ mm, **b** $l_e = 0.01$ mm, 4 snapshots, $\mathbf{l}_s = [0.01, 0.1, 1, 2]$ mm, **c** $l_e = 0.03$ mm, 2 snapshots, $\mathbf{l}_s = [0.1, 1]$ mm, **d** $l_e = 0.03$ mm, 4 snapshots, $\mathbf{l}_s = [0.01, 0.1, 1, 2]$ mm. Only half of the bar is shown due to the symmetry

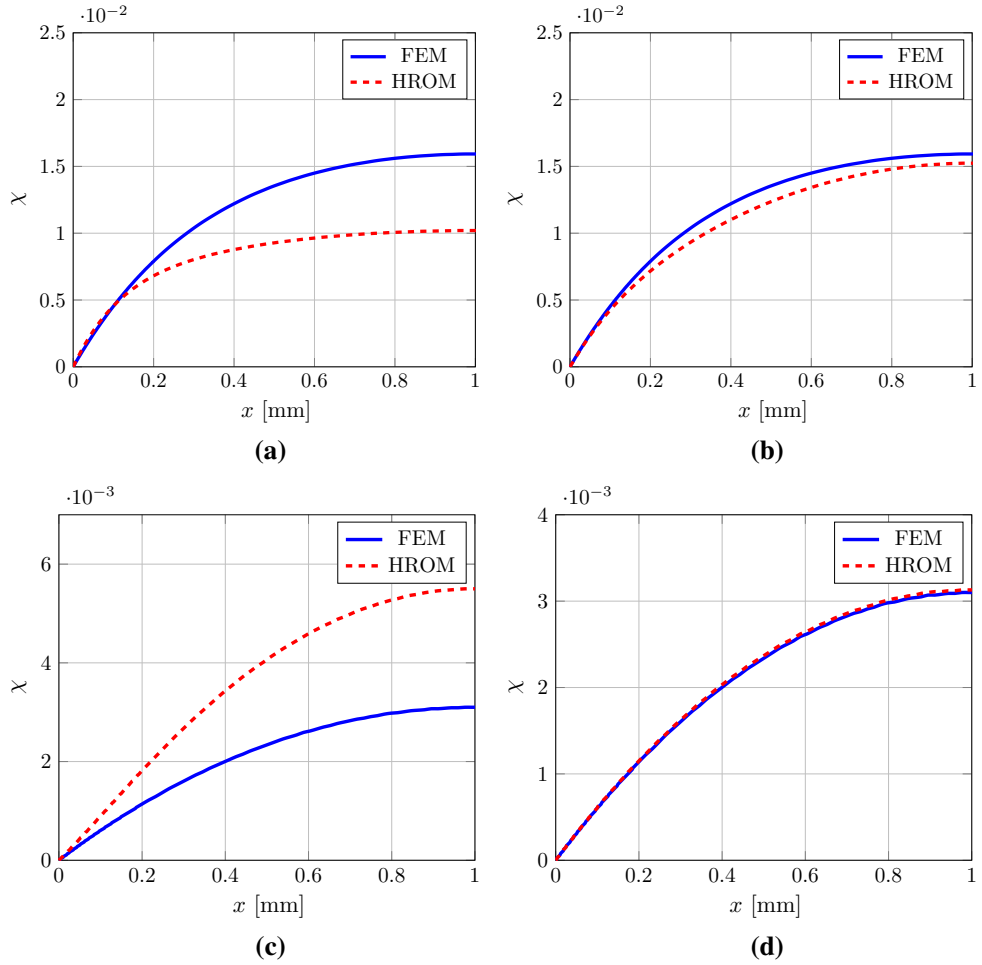

Fig. 16 Clamped tension test: comparison of finite element and hyper-reduced solution of the distribution of the microdilatation field along the bar with L = 2 mm, $\bar{u} = 0.1$ mm: **a** $l_e = 0.3$ mm, 2 snapshots, $\mathbf{l}_s = [0.1, 1]$ mm, **b** $l_e = 0.3$ mm, 4 snapshots, $\mathbf{l}_s = [0.01, 0.1, 1, 2]$ mm, **c** $l_e = 1.5$ mm, 2 snapshots, $\mathbf{l}_s = [0.1, 1]$ mm, **d** $l_e = 1.5$ mm, 4 snapshots, $\mathbf{l}_s = [0.01, 0.1, 1, 2]$ mm. Only half of the bar is shown due to the symmetry

$\nu = 0.4$, $H_\chi = 10^6$ MPa, and $\bar{u} = 0.1$ mm. The same approximation using bi-linear quadrilateral finite element shape functions for displacement as well as for microdilatation degree of freedom was used. The difference between the finite element and hyper-reduced solution along the x-direction in the middle of the height of the bar for different values of the internal length parameter l_e was investigated, that is, $\boldsymbol{\mu} = [l_e]$. This material parameter was ranging from 0.01 mm to 2 mm. The relation (113) between the parameter A_χ and the material length is exploited since definition of the internal length is not known for the clamped tension. The initial snapshots were also taken from the previous example, the vector of snapshot state is $\mathbf{l}_s = [0.1, 1]$ mm.

The HROM solution obtained with two snapshots led to a low error of the displacement field, see Fig. 11a. Nevertheless, the topmost error of the microdilatation degree of freedom exceeded 100%, the error is depicted in Fig. 11b.

Accordingly, error estimator was used to select a new snapshot. The third snapshot was selected as $l_e = 2$ mm. The error together with the error estimator are plotted in Fig. 12a. Obviously, the error was reduced for large values of parameter l_e and remained around the same value for small l_e. For that reason, the procedure was repeated another time. The fourth snapshot was computed for $l_e = 0.01$ mm leading to a small error almost in the whole domain, as is apparent from Figure 12b. The error estimator efficiency is depicted in Fig. 13. Again, the dimension of the reduced basis coincides with the number of snapshots.

Figures 11 and 12 also illustrate differences between POD and hyper-reduced solutions which are related to the selection of the RID illustrated in Fig. 14a for the hyper-reduction with two snapshots and in Fig. 14b for four snapshots. The RID was selected automatically performing DEIM on the reduced basis for DOFs and stresses. Good accuracy were obtained when compared to the full POD even though very small RID

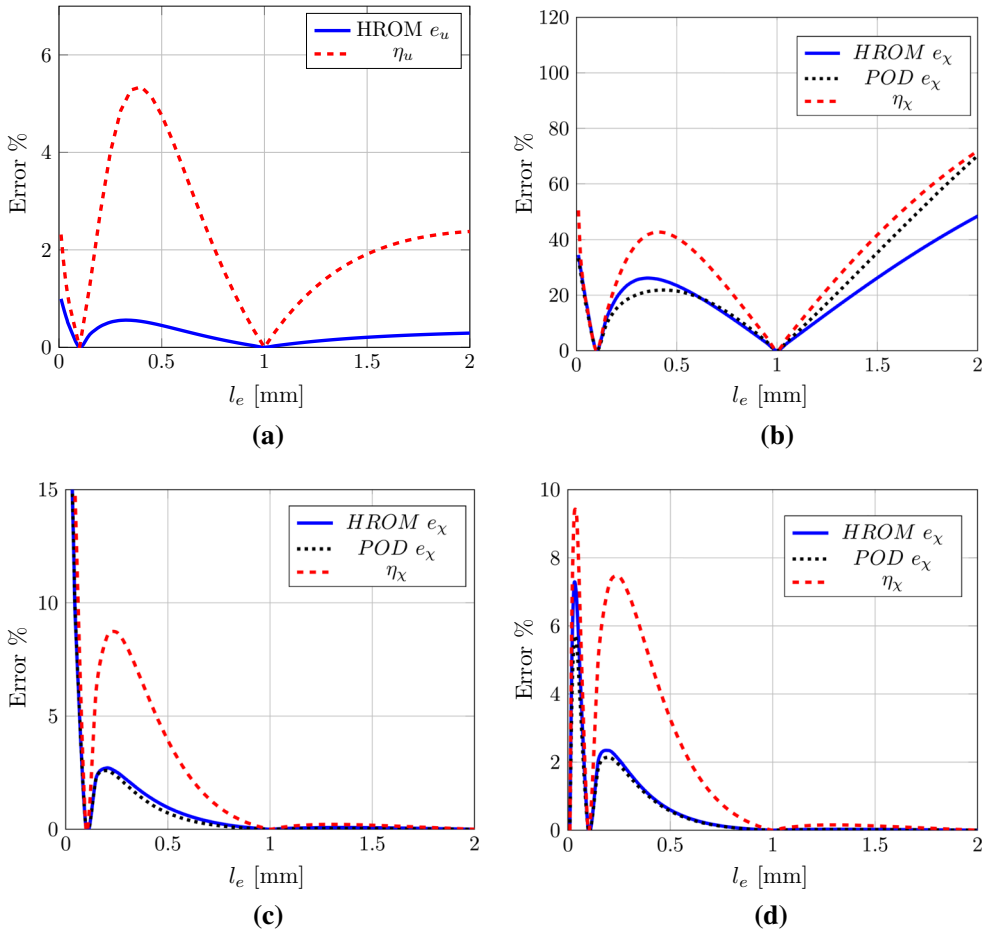

Fig. 17 Error of the hyper-reduced computation of the clamped tension test with separate basis POD: **a** displacement field, 2 snapshots, $\mathbf{l}_s = [0.1, 1]$ mm, **b** microdilatation field, 2 snapshots, $\mathbf{l}_s = [0.1, 1]$ mm, **c** microdilatation field, 3 snapshots, $\mathbf{l}_s = [0.1, 1, 2]$ mm, **d** microdilatation field, 4 snapshots, $\mathbf{l}_s = [0.01, 0.1, 1, 2]$ mm

containing only few elements was selected. Moreover, low computational cost can be expected and will be examined later.

The distribution of the microdilatation field is shown for various cases of internal length in Figs. 15 and 16. The results are again very similar to the example of extension test, i.e. variations of the field can be observed for solutions obtained with two snapshots and the differences between the finite elements and hyper-reduction are nearly identical for four snapshots. The biggest difference can be observed for $l_e = 0.03$ mm which is in accordance with the true and estimated errors.

The influence of the performance of the POD separately for displacements and microdilatations was briefly explored. The same starting points for POD were used. The reduced basis was extracted from two snapshots, $\mathbf{l}_s = [0.1, 1]$ mm. The relative errors for displacements and microdilatation

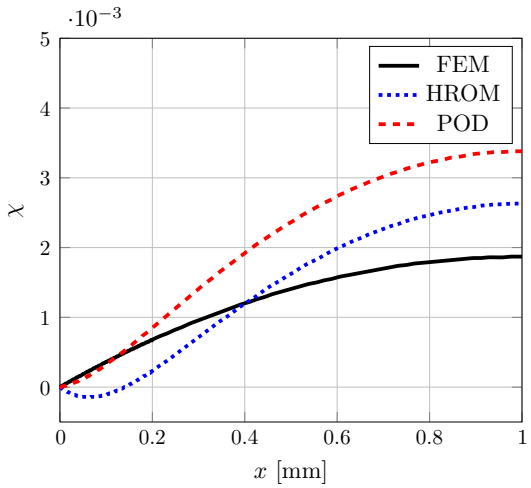

Fig. 18 Clamped tension test. Distribution of the microdilatation field along the bar computed with FEM, POD, and HROM, $l_e = 2$ mm

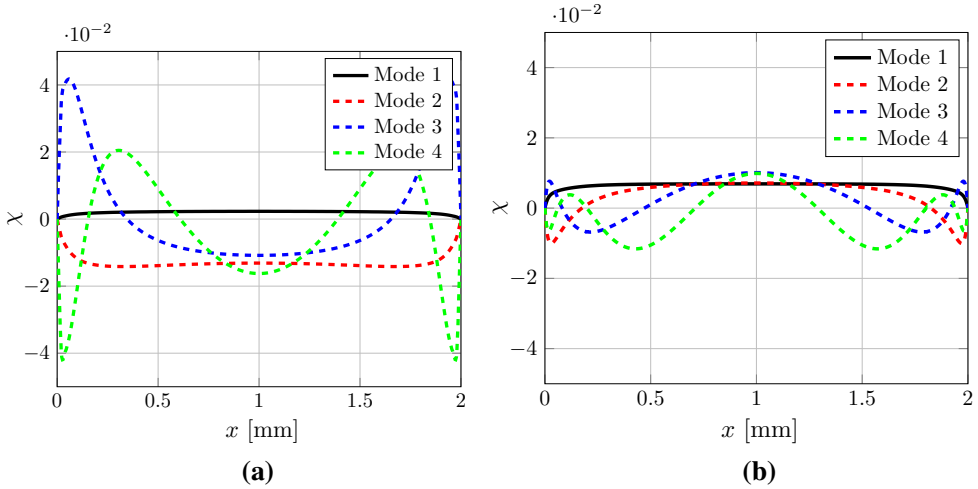

Fig. 19 Clamped tension: microdilatation POD modes. **a** Mixed basis, **b** separated basis

Table 1 Clamped tension: CPU ratio comparison

Number of snapshots	Mixed basis		Separate basis	
	POD	HROM	POD	HROM
2	0.432	0.049	0.442	0.051
3	0.455	0.051	0.476	0.053
4	0.491	0.054	0.521	0.067

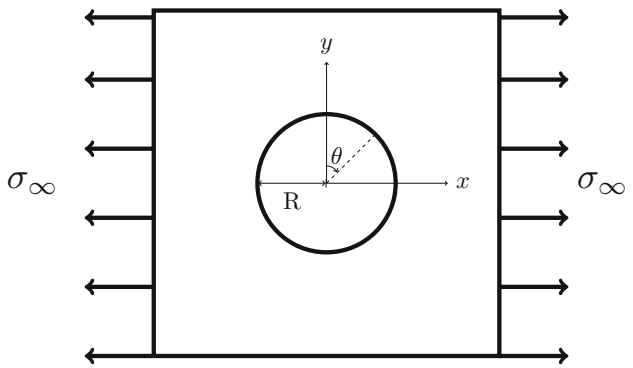

Fig. 20 Stress concentration: problem setting

field are illustrated in Fig. 17a–d. The error of the microdilatation field exceeded 50%. Surprisingly, lower error was obtained with the hyper-reduction than POD. Thus, the profile of the microdilatation field along the bar is plotted for $l_e = 2$ mm in Fig. 18. It can be seen that the hyper-reduced solution leads to a strange behavior close to the boundary resulting in a better match in the middle of the bar and in this manner a lower error. Further, the error was lower just for few hyper-reduced predictions and the norm used for the error does not have strong physical sense.

To improve the solution, new snapshots were added to enhance the reduced space. The third snapshot, $l_e = 2$ mm, and fourth snapshots, $l_e = 0.01$ mm, were gradually added to the basis to obtain relatively low error in the whole domain with results comparable to the mixed basis approach.

Comparison of four POD modes for clamped tension with mixed basis and clamped tension with separated basis can be seen in Fig. 19. Seemingly, only the first mode is similar while other modes are significantly different.

An important aspect of the reduced order model is the computational time of simulations. CPU time between full simulation, POD, and hyper-reduction is compared using

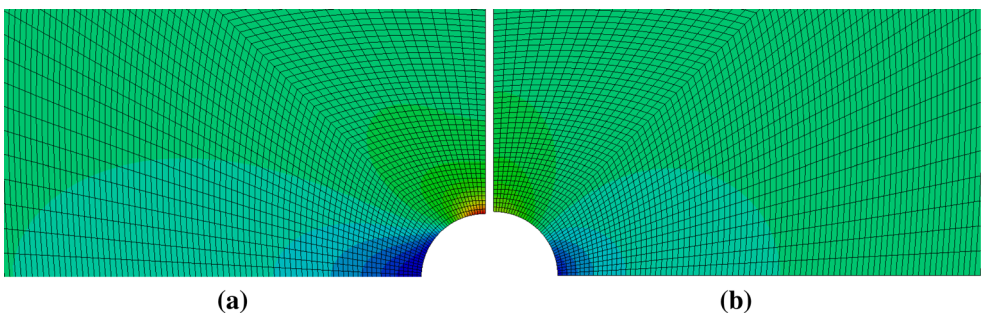

Fig. 21 Stress concentration contour plots around the hole: **a** classical solution, **b** Cosserat elasticity with $l_c = 0$, 1 mm, $R = 1$ mm and $N = 0.9$

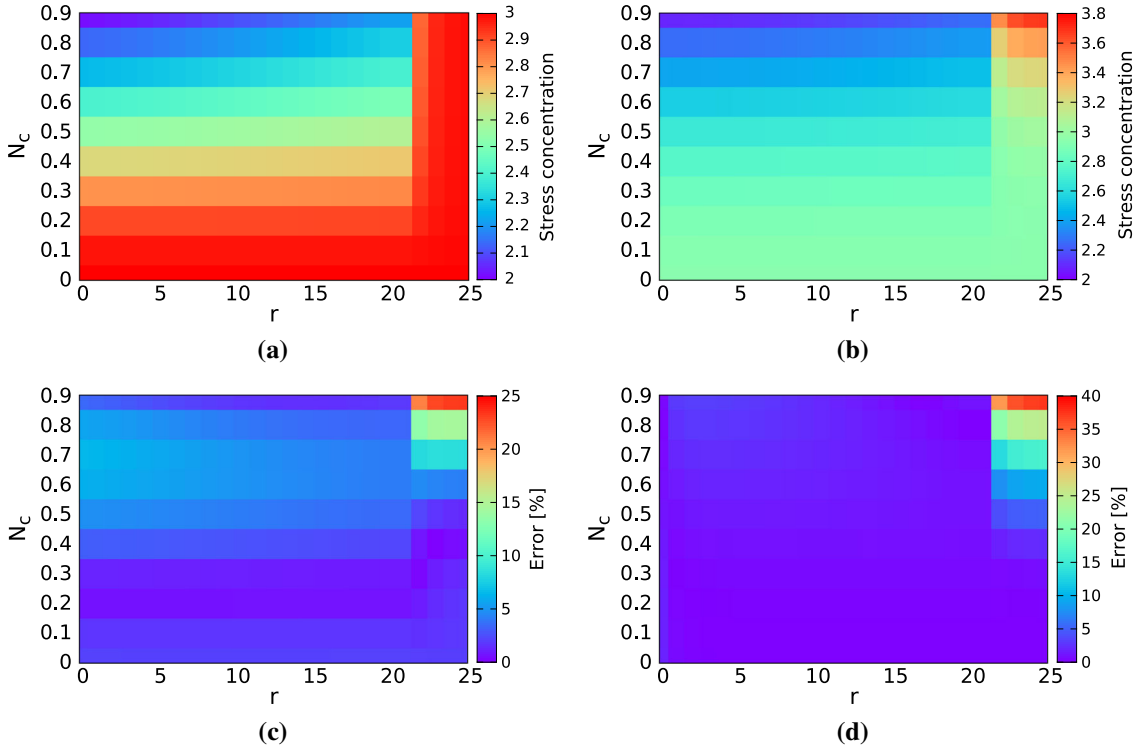

Fig. 22 Stress concentration computed with 4 snapshots: **a** hyper-reduced solutions, **b** analytical solutions, **c** true error, **d** error estimator η

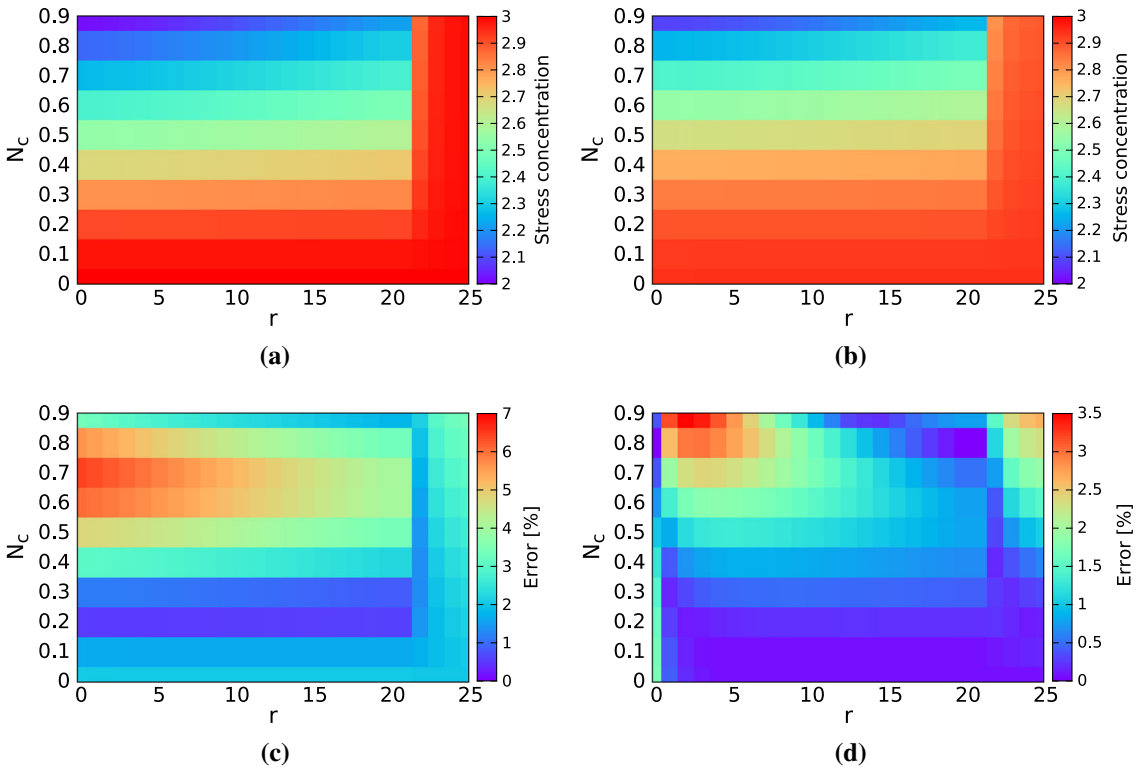

Fig. 23 Stress concentration computed with 6 snapshots: **a** hyper-reduced solutions, **b** analytical solutions, **c** true error, **d** error estimator η

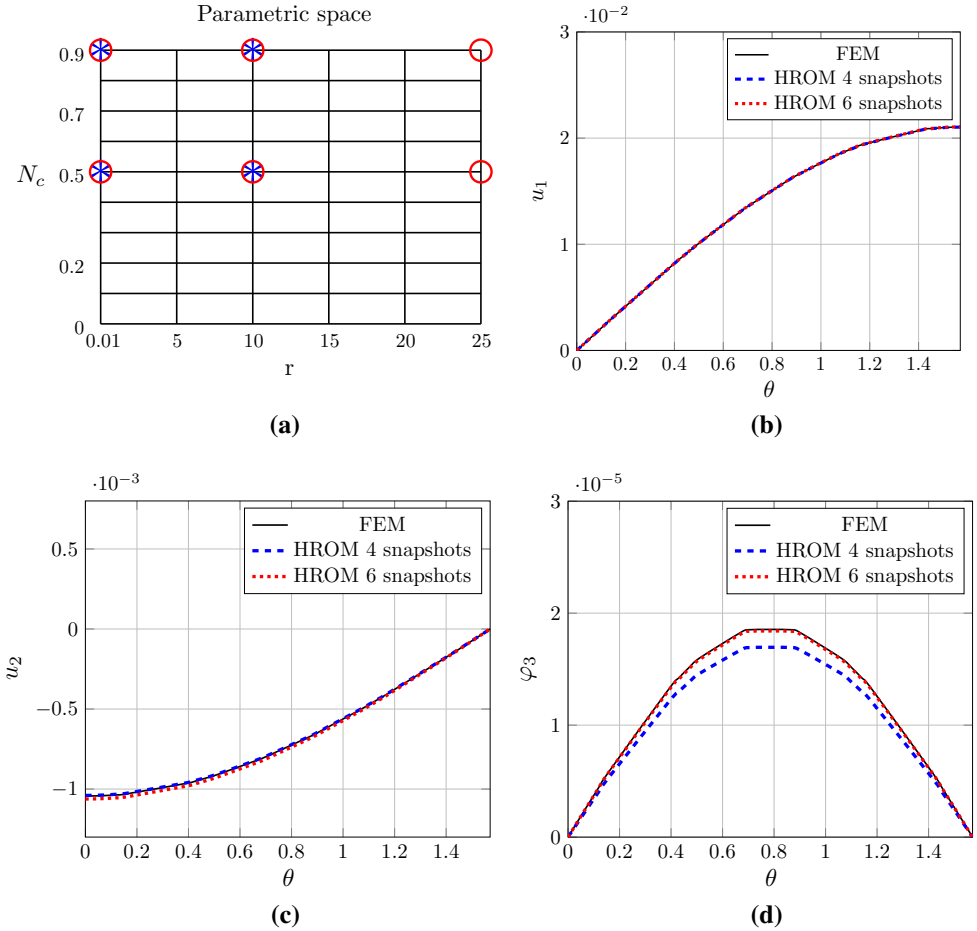

Fig. 24 Stress concentration: **a** parametric space with the selected snapshot points, 4 snapshots case designed with the *red star* and 6 snapshots with the *blue circle*. Distribution along the hole computed with $r = 0.01$, $N = 0.8$: **b** displacement field u_1, **c** displacement field u_2, **d** Cosserat rotation φ_3. (Color figure online)

CPU time ratio as used for example in [31]. The CPU time ratio is defined as the ratio of computational time between reduced-order and full simulation. The results are shown it Table 1.

Clearly, CPU time ratio relies upon the size of the reduced order basis which is directly related to the size of the reduced integration domain. The computational time of the POD method was reduced approximately twice. Much better time saving was obtained with the hyper-reduction method which reduces the POD time roughly by a factor of 10. Thus the speed-up of the hyper-reduced calculations is around 20 with almost the same accuracy of results as the POD.

4.3 Stress concentration in Cosserat elasticity

In the last example the size-dependent concentration factor around a circular hole is studied, viz. Figure 20 for problem setting. Note that the couple tractions are homogeneous. It is well-known that the stress concentration factor around a circular hole is lower for Cosserat continuum than for the classical theory of elasticity [32].

The contour plots of stress concentration for classical and Cosserat elasticity are presented in Fig. 21 to illustrate the difference in the field distributions. Only a part of the domain focusing on the zone with stress concentration is depicted. The field distributions clearly lead to more homogeneous distribution for Cosserat elasticity, see [33] for study of the stress concentration around holes in nickel foams simulated with a micromorphic model. The stress concentration is given as the ratio $\sigma_{11}/\sigma_\infty$ where σ_∞ is the stress component σ_{11} far from the hole. The analytical solution for the stress concentration around a circular hole for the couple-stress theory has been derived in [34] and then extended to the Cosserat elasticity in [32], see also [17,35]. The stress concentration factor at the pole is equal to

$$K_c = \frac{3+F}{1+F} \tag{123}$$

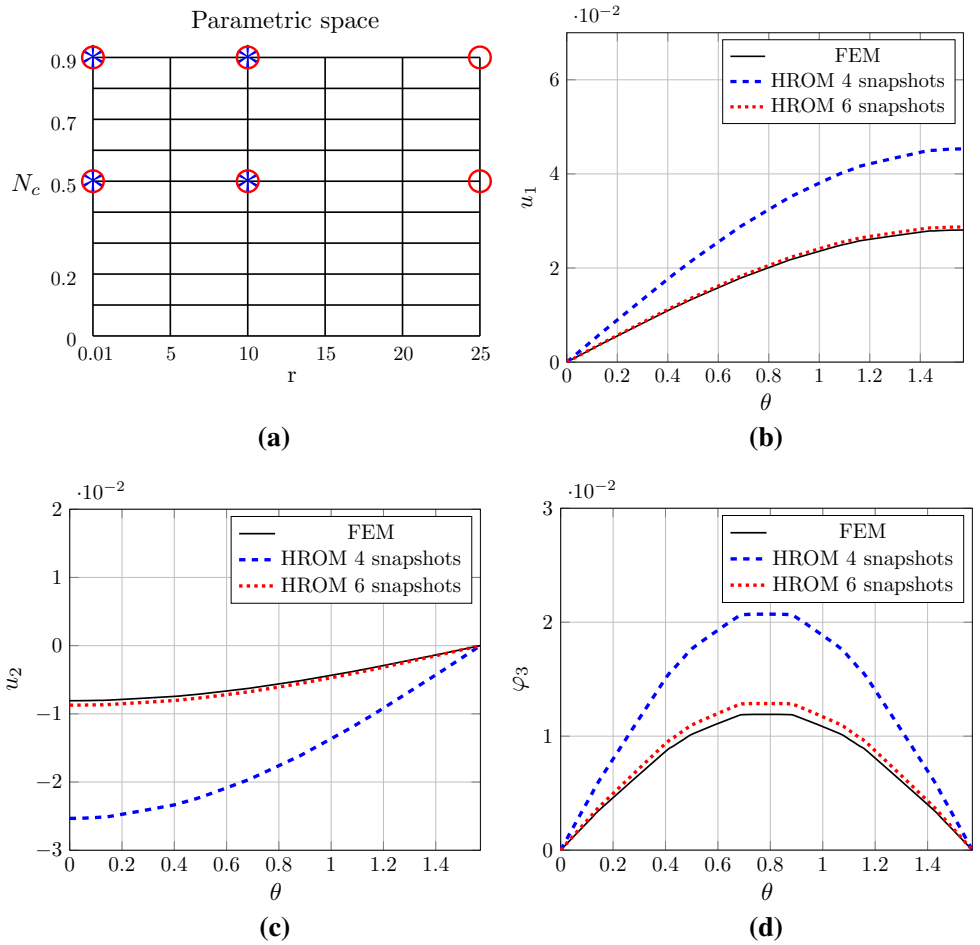

Fig. 25 Stress concentration: **a** parametric space with the selected snapshot points, 4 snapshots case designed with the *red star* and 6 snapshots with the *blue circle*. Distribution along the hole computed with $r = 7$, $N = 0.8$: **b** Displacement field u_1, **c** Displacement field u_2, **d** Cosserat rotation φ_3. (Color figure online)

where

$$F = \frac{8(1-\nu N_c^2)}{4+(rN_c)^2+2rN_c\,[K_0(rN_c)/K_1(rN_c)]} \tag{124}$$

and K_0 and K_1 are the modified Bessel functions of the second kind of order zero and one, respectively, r is a ratio of the radius of the hole R to an internal length scale parameter l_c defined as

$$r = \frac{R}{l_c}, \quad l_c = \sqrt{\frac{A_\chi}{4\mu}} \tag{125}$$

Additionally

$$N_c = \sqrt{\frac{H_\chi}{\mu + H_\chi}} \quad 0 \le N_c \le 1 \tag{126}$$

represents a coupling parameter between the macro problem and Cosserat problem. Note that the couple-stress theory is restored for $N_c = 1$, that is, for $H\chi \to \infty$. The second limit case, $N_c = 0$, leads to two uncoupled problems, thus the stress concentration for classical elasticity is recovered.

Therefore, for the elastic Cosserat continuum, the stress concentration factor depends on the Poisson ratio ν, coupling parameter N_c, and on the ratio r of the radius of the hole to the material length.

The hole problem was simulated using bi-quadratic quadrilateral finite element shape functions for displacements as well as Cosserat degrees of freedom. Owing to the symmetry of the loading and geometry only a quarter of the domain is modeled. Appropriate symmetric boundary condition were applied: $u_2 = 0$ and $\varphi_3 = 0$ on the horizontal axis of symmetry and $u_1 = 0$ and $\varphi_3 = 0$ on the vertical axis of symmetry.

To show the capability of the hyper-reduction, the stress concentration at the pole was explored in a two dimensional

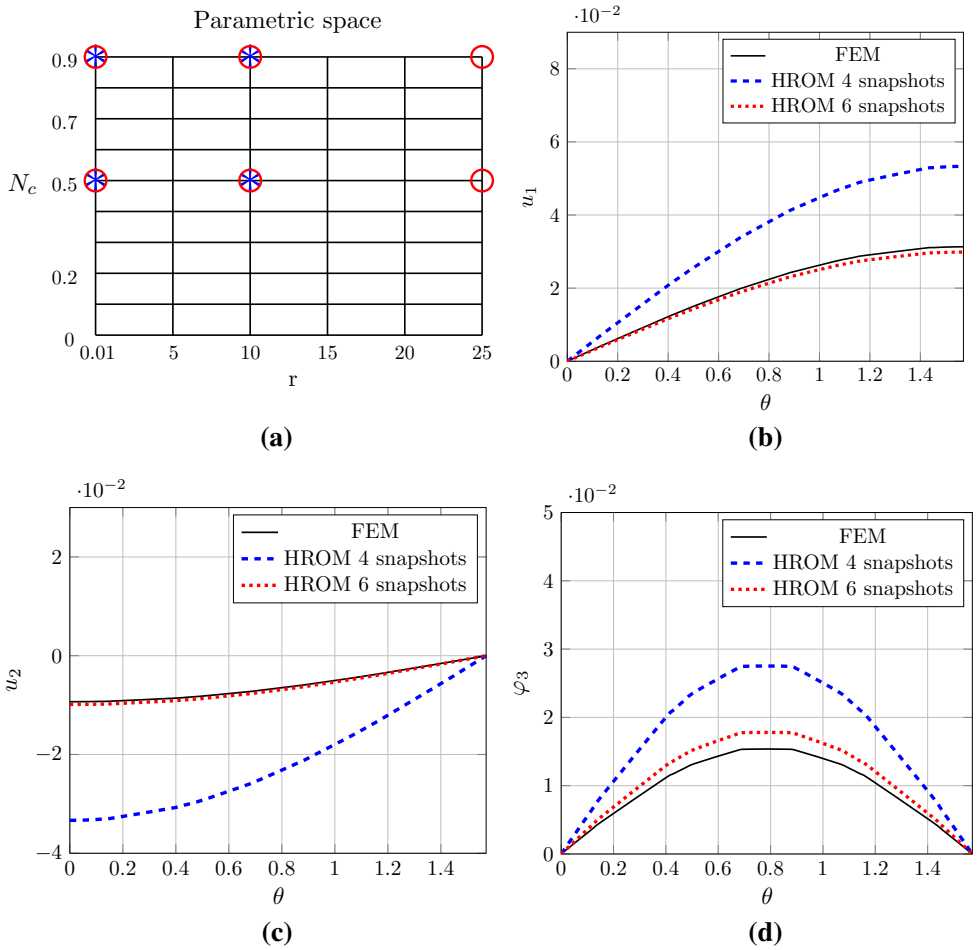

Fig. 26 Stress concentration: **a** Parametric space with the selected snapshot points, 4 snapshots case designed with the *red star* and 6 snapshots with the *blue circle*. Distribution along the hole computed with $r = 25$, $N = 0.8$: **b** displacement field u_1, **c** displacement field u_2, **d** Cosserat rotation φ_3. (Color figure online)

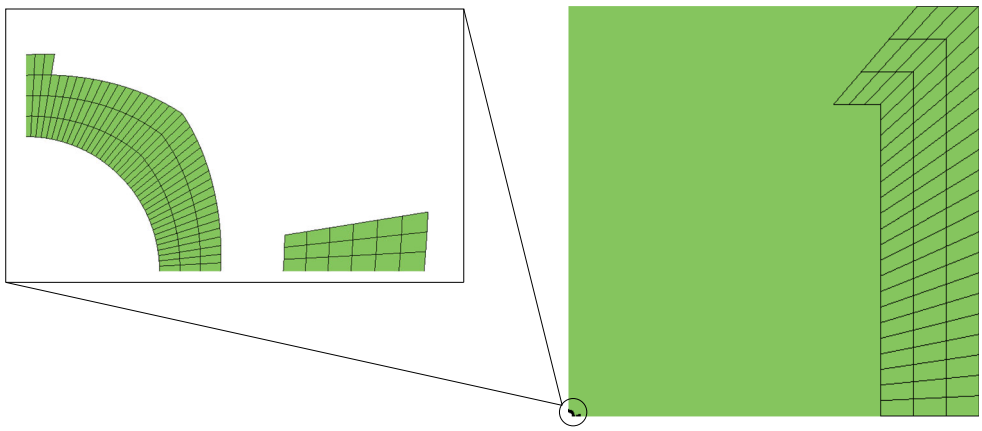

Fig. 27 Stress concentration: reduced integration domain generated by DEIM for four snapshots

parametric space for a wide range of parameters l_c and N_c, namely $\boldsymbol{\mu} = [l_c, N_c]$. The classical material parameters were chosen as $E = 70{,}000$ MPa, $\nu = 0.4$ while Cosserat material parameters were varied, N_c from 0 to 0.9 and l_c from 0.04 mm to 200 mm which for fixed radius of the hole $R = 1$ mm corresponds to the variation of parameter r between 0.005 and 25. First, the capability of the hyper-reduction with mixed basis POD to predict the concentration factor was evaluated

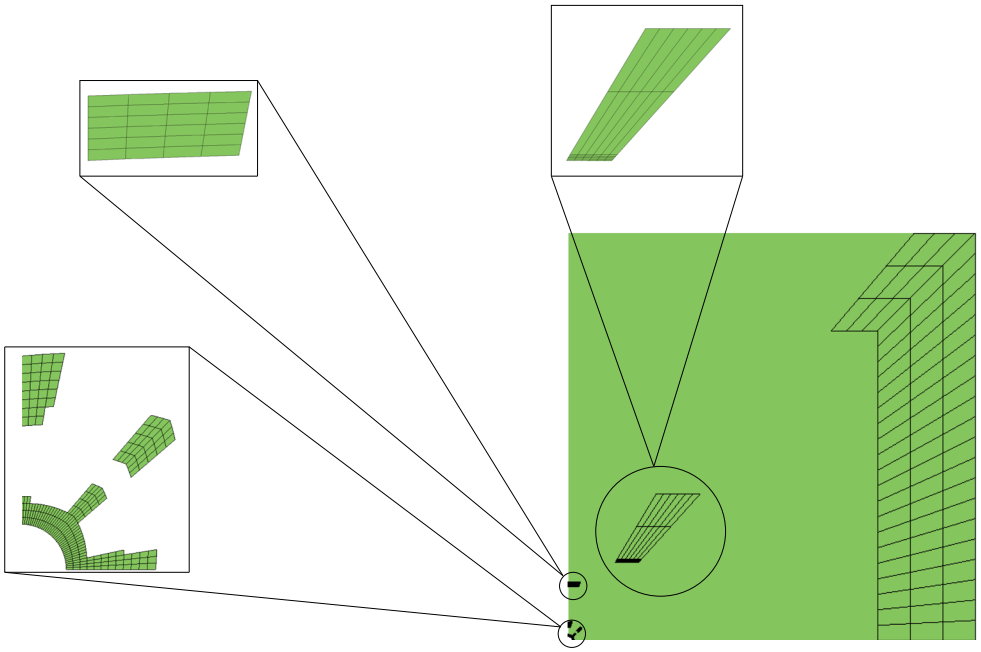

Fig. 28 Stress concentration: reduced integration domain generated by DEIM for six snapshots

using 4 snapshots. The snapshots were chosen as permutations of components of parameter vectors $\mathbf{l}_s = [0.1, 100]$ mm and $\mathbf{N}_s = [0.5, 0.9]$. Figure 22a shows the stress concentration obtained by the hyper-reduced simulations. The results are in a good agreement with the analytical results in a big part of the parametric space, see Fig. 22b, c. However, the error exceeded 25% in a right upper part of the parametric domain which was also correctly predicted by the error estimator plotted in Fig. 22d. Note that to estimate the error of the stress concentration, the maximum of values defined in (105) and (106) is used, i.e., $\eta = \max(\eta_u, \eta_\chi)$. Correspondingly, based on the error estimator, the parametric vector $\mathbf{l}_s$ was enhanced by $l_c = 0.04$ mm, thus six snapshots were collected. Besides that the dimension of the reduced bases again coincide with the number of snapshots in both cases.

The six snapshots hyper-reduced solutions are depicted in Fig. 23a. The accuracy of the hyper-reduction is assessed in Fig. 23c where the difference between the hyper-reduced and analytical solutions are compared. Note that this error contains also the finite element error related to the discretization. The estimated error is illustrated in Fig. 23d. It is apparent that the hyper-reduced simulations give accurate estimations of the stress concentration factor; moreover, the error estimator provides a good approximation of the validity domain.

To explore the results deeper, distributions of the displacements and Cosserat rotation along the hole for different values of the internal length and its comparison with finite element solutions is depicted in Figs. 24, 25 and 26. The position is specified by θ which is an angle measured from the vertical axis in the clockwise direction, see Fig. 20. Seemingly, the solutions obtained with four snapshots are

Table 2 Stress concentration: CPU ratio comparison

Number of snapshots	POD	Hyper-reduction
4	0.432	0.124
6	0.491	0.171

comparable with the finite element simulation for $N_c = 0.8$ and $r = 0.01$, still, considerably different for $r = 7$ and $r = 25$. A good agreement was achieved with six snapshots for all cases as was predicted by the error estimator. Comparison of the reduced integration domains for the first and second case can be seen in Figs. 27 and 28. The reduced integration domain was assembled automatically applying the DEIM technique on the reduced basis for degrees of freedom and stresses, as a result, the reduced integration domain is larger for the second case which reduced basis has a bigger dimension. Finally, comparison of the CPU ratio between the POD and hyper-reduction was evaluated. The results are summarized in Table 2. The speed-up of the simulation is around 6 for the hyper-reduction method and approximately 2 for POD.

Finally, the size-dependent concentration factor is explored using the separated basis POD with the hyper-reduction. The same simulations as in the previous section are repeated and the results for the case with 4 snapshots can be seen in Fig. 29a–d. In comparison with Fig. 22a–d the separate basis approach leads to more accurate results with maximal estimated error around 14%.

As was already stated the physical meaning of constraining micromorphic degrees of freedom is a difficult topic that depends on the specific physical content of the model. For

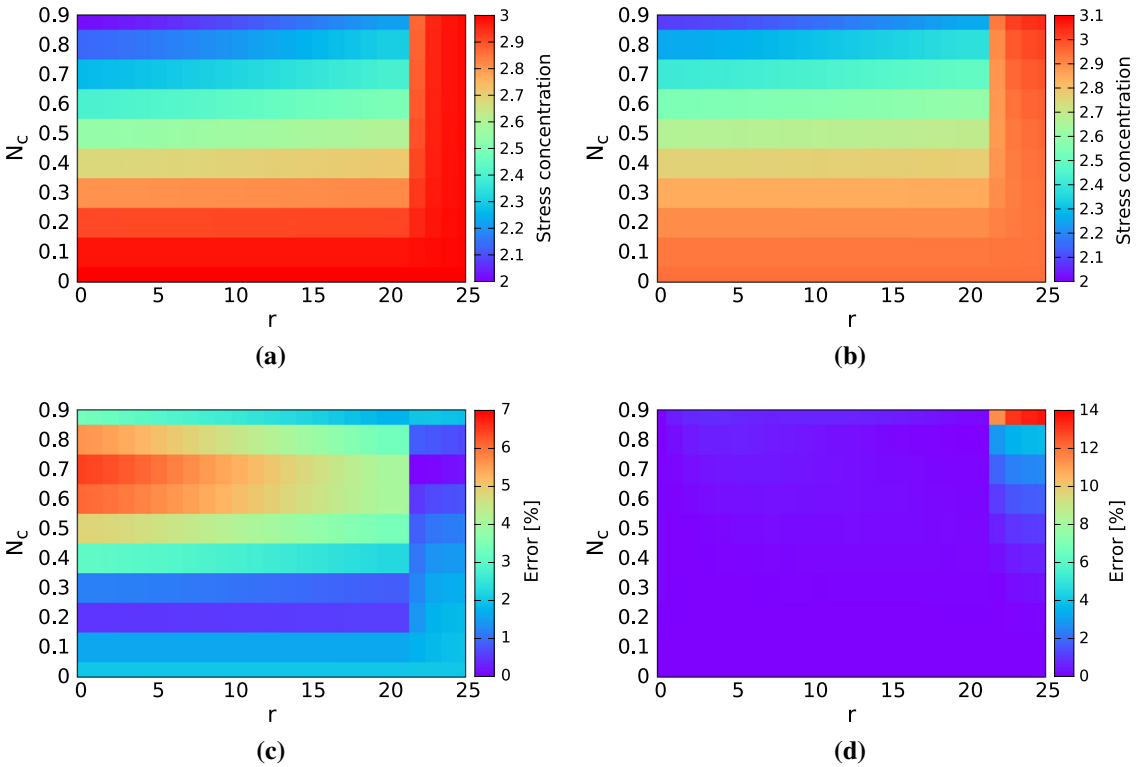

Fig. 29 Stress concentration: **a** hyper-reduced solutions, **b** analytical solutions, **c** true error, **d** error estimator η

instance, in the context of metal plasticity, it amounts to preventing dislocations to occur at this surface due to passivation effect. In the examples of Sects. 4.1 and 4.2, the micromorphic variable is constrained at the boundary in order to trigger a non-homogeneous boundary layer effect. In these examples, Neumann boundary conditions with vanishing higher order traction would lead to the classical homogeneous solution. In Cosserat example Sect. 4.3, the boundary layer effect is induced by the stress concentration so that Neumann conditions for higher order tractions are used around the hole because this is a free surface. Far from the hole the boundary conditions are such that the fields remain homogeneous.

5 Conclusions

In the present paper, to our best knowledge the first reduced order modeling of general linear micromorphic continua has been introduced. The approach is general in the sense that it can be applied to a large class of generalized continua, namely to micromorphic continua with different number of additional degrees of freedom ranging form 1 to 9, including the microdilatational and Cosserat cases treated in the paper. The POD together with the hyper-reduction method were introduced and applied to three examples. The POD method was used to create the reduced basis. Moreover, two approaches were explored in the context of creation of reduced bases from two set of degrees of freedom with different physical meaning. Both of them leading to similar results. It was shown that the structure of the hyper-reduced approximation and assemblage of the reduced domain preserves the structure of classical continuum, the equations are just enhanced by micromrophic fields. The hyper-reduction was applied to parametric study of the internal length parameter in microdilatation extension and clamped tension. The error estimator was introduced which enables to adaptively increase the dimension of the reduced space by adding new snapshots in case of large error. Accurate results were obtained with substantial reduction of computational time. The final example explores size-dependent stress concentration in Cosserat elasticity. Two parameter study was performed and accurate values of stress concentration were achieved with four snapshots within a part of the parametric space. To extend the validity domain, the reduced space was enhanced by two snapshots which selection was based on the error estimator. Finally, a good agreement between the analytical and hyper-reduced solution were obtained and the computational time was accelerated by a factor of 6. In all presented examples, the RID is focused on regions with significant gradient of micromorphic variables. This concerns only very few elements of the original mesh.

Application of the hyper-reduction to micromorphic models with gradient of internal variables which serves as

localization limiters will be addressed in a separate paper. The method of separate basis would be probably preferable.

Acknowledgements This study was carried out in the framework of project MICROMORFING (ANR-14-CE07-0035-03) funded by the Agence Nationale de la Recherche (ANR, France). This support is gratefully acknowledged.

References

1. Mindlin RD (1964) Micro-structure in linear elasticity. Arch Ration Mech Anal 16:3
2. Eringen AC, Suhubi E (1964) Nonlinear theory of simple micro-elastic solids—I. Int J Eng Sci 2(2):189–203
3. Eringen AC, Suhubi E (1964) Nonlinear theory of simple micro-elastic solids—II. Int J Eng Sci 2(2):389–404
4. Forest S, Sievert R (2006) Nonlinear microstrain theories. Int J Solids Struct 43(24):7224–7245
5. Almroth B, Stern P, Brogan F (1978) Automatic choice of global shape functions in structural analysis. AIAA Journal 16(5):525–528
6. Cuong NN, Veroy K, Patera AT (2005) Certified real-time solution of parametrized partial differential equations. In: Sidney Y (ed) Handbook of materials modeling: methods. Springer, Dordrecht, pp 1529–1564
7. Ryckelynck D (2005) A priori hyperreduction method: an adaptive approach. J Comput Phys 202(1):346–366
8. Ryckelynck D (2009) Hyper-reduction of mechanical models involving internal variables. Int J Numer Methods Eng 77(1):75–89
9. Ryckelynck D (2009) Hyper reduction of finite strain elasto-plastic models. Int J Mater Form 2(1):567–571
10. Hernández J, Oliver J, Huespe AE, Caicedo M, Cante J (2014) High-performance model reduction techniques in computational multiscale homogenization. Comput Methods Appl Mech Eng 276:149–189
11. Georgiou I (2005) Advanced proper orthogonal decomposition tools: using reduced order models to identify normal modes of vibration and slow invariant manifolds in the dynamics of planar nonlinear rods. Nonlinear Dyn 41(1–3):69–110
12. Farhat C, Avery P, Chapman T, Cortial J (2014) Dimensional reduction of nonlinear finite element dynamic models with finite rotations and energy-based mesh sampling and weighting for computational efficiency. Int J Numer Methods Eng 98(9):625–662
13. Forest S (2009) Micromorphic approach for gradient elasticity, viscoplasticity, and damage. J Eng Mech 135(3):117–131
14. Germain P (1973) La méthode des puissances virtuelles en mécanique des milieux continus. J Méc 12:236–274
15. Germain P (1973) The method of virtual power in continuum mechanics. Part 2: Microstructure. SIAM J Appl Math 25(3):556–575
16. Auffray N, Le Quang H, He Q-C (2013) Matrix representations for 3d strain-gradient elasticity. J Mech Phys Solids 61(5):1202–1223
17. Eringen AC (1968) Mechanics of micromorphic continua. In Kröner E (ed) Mechanics of generalized continua: proceedings of the IUTAM-Symposium on The Generalized Cosserat Continuum and the Continuum Theory of Dislocations with Applications, Freudenstadt and Stuttgart (Germany) 1967. Springer, Berlin, pp 18–35
18. Goodman M, Cowin S (1972) A continuum theory for granular materials. Arch Ration Mech Anal 44(4):249–266
19. Cosserat E, Cosserat F (1909) Théorie des corps déformables. Paris 3:17–29
20. Besson J, Cailletaud G, Chaboche J-L, Forest S (2009) Non-linear mechanics of materials, vol 167. Springer, Berlin
21. Sirovich L (1987) Turbulence and the dynamics of coherent structures. Part I: Coherent structures. Q Appl Math 45(3):561–571
22. Iollo A, Lanteri S, Désidéri J-A (2000) Stability properties of POD-Galerkin approximations for the compressible Navier–Stokes equations. Theor Comput Fluid Dyn 13(6):377–396
23. Lutowska A (2012) Model order reduction for coupled systems using low-rank approximations. PhD thesis, Eindhoven University of Technology
24. Fritzen F, Hodapp M, Leuschner M (2014) GPU accelerated computational homogenization based on a variational approach in a reduced basis framework. Comput Methods Appl Mech Eng 278:186–217
25. Chaturantabut S, Sorensen DC (2010) Nonlinear model reduction via discrete empirical interpolation. SIAM J Sci Comput 32(5):2737–2764
26. Maday Y, Rønquist EM (2002) A reduced-basis element method. J Sci Comput 17(1–4):447–459
27. Ryckelynck D, Gallimard L, Jules S (2015) Estimation of the validity domain of hyper-reduction approximations in generalized standard elastoviscoplasticity. Adv Model Simul Eng Sci 2(1):1
28. Patzák B, Bittnar Z (2001) Design of object oriented finite element code. Adv Eng Softw 32(10):759–767
29. Patzák B (2012) OOFEM—an object-oriented simulation tool for advanced modeling of materials and structures. Acta Polytech 52(6):59–66
30. Horák M, Patzák B, Jirásek M (2014) On design of element evaluators in OOFEM. Adv Eng Softw 72:193–202
31. Radermacher A, Reese S (2014) Model reduction in elastoplasticity: proper orthogonal decomposition combined with adaptive sub-structuring. Comput Mech 54(3):677–687
32. Kaloni PN, Ariman T (1967) Stress concentration effects in micropolar elasticity. Z Angew Math Phys 18(1):136–141
33. Dillard T, Forest S, Ienny P (2006) Micromorphic continuum modelling of the deformation and fracture behaviour of nickel foams. Eur J Mech A Solids 25(3):526–549
34. Mindlin R (1963) Influence of couple-stresses on stress concentrations. Exp Mech 3(1):1–7
35. Cowin SC (1970) An incorrect inequality in micropolar elasticity theory. Z Angew Math Phys 21(3):494–497